Engineering xxx (xxxx) xxx

Contents lists available at ScienceDirect

Engineering

journal homepage: www.elsevier.com/locate/eng

Research
Energy System Engineering—Article

Multi-Timescale Scheduling Optimization of ALK/PEM Hybrid Electrolyzers System Considering Flexible Hydrogen Demand

Bowen Wang [a,b], Zhaoqing Liang [a], Kai Yang [a], Lei Xing [c], Heng Shao [d], Zhuorui Wu [b], Yixin Liu [b,e], Li Guo [b,e], Ning Yang [f], Bing Hu [g], Chengshan Wang [b,e], Kui Jiao [a,b,*]

[a] State Key Laboratory of Engines, Tianjin University, Tianjin 300350, China
[b] National Industry-Education Platform for Energy Storage, Tianjin University, Tianjin 300350, China
[c] School of Chemistry and Chemical Engineering, University of Surrey, Guildford GU2 7XH, UK
[d] Shanghai H-Rise New Energy Technology Co., Ltd., Shanghai 201413, China
[e] State key laboratory of Intelligent Power Distribution Equipment and System, Tianjin University, Tianjin 300350, China
[f] School of Energy Resource and Power Engineering, Northeast Electric Power University, Jilin 132012, China
[g] School of Control Engineering, Xinjiang Institute of Engineering, Urumqi 830023, China

ARTICLE INFO

Article history:
Received 26 October 2025
Revised 27 January 2026
Accepted 27 February 2026
Available online xxxx

Keywords:
Hydrogen production from renewable energy
Hybrid electrolyzers system
Multi-timescale rolling optimization
Flexible hydrogen load demand
Joint wind-photovoltaic power prediction

ABSTRACT

Hydrogen production from renewable energy is a promising solution for clean and efficient hydrogen generation. The hybrid electrolyzers system (HES) consists of alkaline (ALK) and proton exchange membrane (PEM) electrolyzers. It balances PEM's economic benefits and ALK's hydrogen production capabilities. To enhance hydrogen production efficiency and ensure the operational stability of HES, this study proposes a novel multi-timescale rolling optimization strategy considering flexible hydrogen demand. A joint wind–photovoltaic power prediction model is used to provide accurate forecast data for scheduling optimization. The operating characteristics of the electrolyzers, including various operating states, start–stop behaviors, load variations, and hydrogen production features of ALK and PEM, are modeled in detail. Multi-timescale modeling is employed for rolling optimization to obtain the optimal scheduling solution. Finally, the validity of the proposed method is verified under varying weather types in Macheng, Hubei, China. The results show that HES significantly improves hydrogen production capacity and economics compared to ALK-only production, with a 25% increase in net revenue under extreme weather. Flexible hydrogen load demand response synchronizes fluctuations on both the supply and demand sides, multiplying grid trading benefits. The multi-timescale scheduling strategy enabled each electrolyzer to achieve over 96% execution of the day-ahead schedule across various weather conditions. The system's economy achieves 98% of the ideal maximum benefit and 80% under extreme weather. This demonstrates that the proposed scheme holds promise for providing effective solutions for the optimal design and scheduling of renewable energy hydrogen production systems.

1. Introduction

Energy scarcity, environmental pollution, and climate change are significant global challenges today [1]. Efficient, low-carbon, environmentally friendly, safe, and reliable energy is in increasing demand. Thus, fundamental changes are needed for the current fossil fuel-dependent energy mix [2]. Renewable energy sources (RES) such as solar and wind power are expected to be the mainstay of future energy supply [3]. Projections suggest that renewable energy will account for 40% of total electricity generation by 2040 [4]. However, both wind and solar energy are highly intermittent and volatile, making large-scale grid integration a major challenge as renewable energy penetration increases [2,5]. Additionally, substantial amounts of wind and solar energy are often wasted due to disparities in population distribution, geography, inadequate grid connectivity, and unequal utilization of renewable energy [6]. An effective energy carrier is urgently needed to facilitate the sustainable transition to renewable energy. Hydrogen energy, with its high energy density and ease of storage

* Corresponding author at: State Key Laboratory of Engines, Tianjin University, Tianjin 300350, China; National Industry-Education Platform for Energy Storage, Tianjin University, Tianjin 300350, China.
E-mail address: kjiao@tju.edu.cn (K. Jiao).

https://doi.org/10.1016/j.eng.2026.02.020

Please cite this article as: B. Wang, Z. Liang, K. Yang et al., Multi-Timescale Scheduling Optimization of ALK/PEM Hybrid Electrolyzers System Considering Flexible Hydrogen Demand, Engineering, https://doi.org/10.1016/j.eng.2026.02.020

and transport, plays a key role in promoting renewable energy utilization [7,8]. Furthermore, hydrogen energy has significant potential across various energy development and utilization scenarios due to its environmentally friendly nature [9,10].

Global hydrogen demand is projected to increase by 2.4 times (211 Mt) in 2030 and 6.0 times (528 Mt) in 2050, as the use of hydrogen energy expands worldwide [11]. To meet global decarbonization targets and address the rising demand for green hydrogen, electrolyzer hydrogen production technology is widely used in renewable hydrogen projects [12]. Electrolytic hydrogen production devices can be classified into three categories based on the electrolytes used: ALK electrolyzers [13], PEM electrolyzers [14], and solid oxide electrolytic cells (SOECs) [15]. SOEC still faces many limitations for large-scale applications, while ALK and PEM electrolyzers are favored for their unique advantages. The PEM, with its broader power range and faster response time, is particularly suitable for flexible operation [16]. Additionally, compact PEM typically exhibits higher current densities and hydrogen production efficiencies, enabling efficient operation at lower temperatures to produce high-purity hydrogen [17]. However, the high manufacturing costs have limited the large-scale application of PEM [5]. In contrast, ALK dominates the market due to its affordability, scalability, and established technology [12].

Safety is a primary concern in practical ALK application projects. Operating under low power conditions, gas interactions, and delays in responding to power fluctuations can increase the risk of explosion [18]. Consequently, ALKs are operated at more than 40% of their rated power in practical applications to minimize the risk of explosion [19]. However, power from wind turbines (WT) and photovoltaic (PV) systems can reach hundreds of megawatts (MW), and a single electrolyzer cannot efficiently dissipate such large input power [12]. Thus, deploying ALK arrays under real-world conditions with high power lower limits can lead to idle electrolyzers and frequent start-ups and shutdowns. This significantly reduces the hydrogen production efficiency and renewable energy consumption rate of the renewable energy hydrogen production system (REHPS). In summary, balancing safety protocols with hydrogen production capacity remains the main challenge for REHPS in practice.

1.1. Literature review

Numerous methods have been developed for co-optimization in REHPS in previous studies [7–9,19–23]. These methods typically set constraints for either ALK or PEM and optimize the solution for the respective objective function [24]. For details, refer to the selected literature review in Table 1 [5,7–9,12,18–23,25–29]. These studies aim to couple additional modules such as battery energy storage system (BESS), hydrogen energy storage system (HESS), and main grid (MG) to maximize the hydrogen production capacity of the system. Despite extensive research on optimizing ALK for hydrogen production, challenges persist in scenarios involving renewable energy integration due to the inherent characteristics of ALK. In contrast, PEM demonstrates good compatibility with RES. By fully leveraging the efficient and flexible characteristics of PEM, the energy utilization and hydrogen production capacity of the electrolysis system can be optimized [30]. This suggests that ALK and PEM have the potential for economic and technological complementarity [25]. If the two electrolyzers are applied together in the same REHPS, the challenge of balancing hydrogen production capacity and economic efficiency can be resolved. Therefore, the hybrid electrolyzers system (HES), which integrates ALK and PEM under a high proportion of RES, is highly significant for research and application in large-scale hydrogen production and low-carbon energy supply.

A review of the remaining literature in Table 1 reveals that preliminary studies on HES have been conducted consecutively [5,7–9,12,18–23,25–29]. Yang et al. [5] and Zhang et al. [12] optimized the scheduling of a hydrogen production system integrating ALK and PEM electrolyzers using different co-optimization algorithms, aiming to efficiently manage the operation strategies of each electrolyzer. The loads, switching actions, and operating times of the electrolyzers were balanced, in contrast to simple sequential and rotational strategies. Xu et al. [18] demonstrated that the hydrogen production capacity of the system was optimized when PEM-installed loads were within the range of 10–20% of the HES. Additionally, the impact of the proportion of wind power and purchased power on the system's economics was analyzed. Dong et al. [25] proposed a PV–wind–hydropower–hydrogen cogeneration system model, offering a solution for the simultaneous design and optimization of HES scheduling. Zheng et al. [26] and Lin et al. [27] combined the dynamic operational response characteristics of ALK and PEM to explore the impact of integrating the advantages of both electrolyzers into HES for REHPS. The results showed that the system significantly improved renewable energy utilization and economic benefits compared to using a single ALK or PEM. Lu et al. [28] proposed a dynamic power allocation and control strategy for HES, accurately allocating fluctuation components between ALK and PEM by reconstructing the fluctuating power of the RES. This strategy improved the source–load balance and increased hydrogen production efficiency by 7% while reducing the electrolyzer capacity requirement. Yu et al. [29] additionally considered the island's wave energy and the utilization of ALK waste heat, optimizing HES scheduling using a two-layer fuzzy control approach. The results showed that the system's annual return and equipment life were significantly improved.

In general, most studies on HES have focused on the macro-level system, primarily addressing the configuration of individual capacities and the variation of annual gains over long time scales. There is a lack of detailed modeling of the dynamic processes and variable load characteristics of hydrogen production for ALK and PEM. Under long-term operation plans, the operation status and economic benefits of electrolyzers in HES with small intraday time scales are not effectively optimized and lack robustness. Moreover, studies often neglect the accurate representation of individual electrolyzer states. Although several studies have evaluated the operating states of individual electrolyzers, they do not represent true operating conditions at their respective time scales, and no literature comprehensively considers both ALK and PEM states. Additionally, these studies do not adequately account for intraday forecast errors caused by renewable energy uncertainty, limiting the resilience potential of HES to various disturbances. This also contributes to the lack of attention paid to the ability of individual electrolyzers in HES to operate stably. Additionally, most studies focus on optimizing the total system yield for a given hydrogen load (HL) demand, without considering the impact of flexible hydrogen demand on system operation and economics. Finally, the balance between the feasibility of the scheduling strategy and solution efficiency under the system's complex multi-constraints has also been overlooked. Therefore, it is necessary to design a scheduling optimization strategy that accurately schedules and optimally adjusts the load and variable load characteristics of each electrolyzer for stable operation in HES, ensuring efficient and smooth hydrogen production. This will maximize the economic efficiency and operational stability of the hydrogen production system.

1.2. Research contributions

Based on the analysis in the previous section, it is evident that the field of HES is still in its early stages and lacks accurate model-

Table 1
Literature reviews on coordinated scheduling optimization of REHPS.

Ref.	Component					HLDR	Time scale	Objectives	Operating characteristics of electrolyzer	
	PV	WT	ALK	PEM	Others				Single status	Operational stability
[5]	√	√	√	√	—	×	15 min	HPR, LPSP	√	×
[7]	√	√	×	√	HESS, FC, MG	×	hour	LCOH	×	×
[8]	×	√	×	√	HESS	×	hour	LOEE	√	×
[9]	√	√	×	√	HESS, FC	×	hour	LOEE	×	×
[12]	√	√	√	√	BESS	×	hour	HPR	√	×
[18]	√	√	√	√	BESS, HESS, MG	×	hour	NPV	√	×
[19]	√	√	√	×	BESS, HESS, FC, SC	×	min	LOEE	×	×
[20]	√	√	√	×	BESS	×	hour	LCOH	×	×
[21]	√	×	√	√	BESS, HESS, FC	×	hour	LCOE	×	×
[22]	√	√	√	×	HESS, MG, CP	×	hour	DNPV	×	×
[23]	√	√	×	√	BESS, HESS, MG, PS	×	hour	NPV, LPSP, LOEE	×	×
[25]	√	√	√	√	HESS, MG, HPS	×	hour	NPV	×	×
[26]	√	√	√	√	—	×	hour	LCOH, LPSP	×	×
[27]	×	√	√	√	HESS	×	hour	AOP	×	×
[28]	√	√	√	√	BESS	×	10 min	LPSP, LOEE, HPR	√	×
[29]	√	√	√	√	HESS, TESS, WPS	×	hour	AOP	×	×
This work	√	√	√	√	BESS, HESS, MG	√	Multi-timescale	DNPV	√	√

HESS: hydrogen energy storage system; FC: fuel cell; MG: main grid; BESS: battery energy storage system; SC: supercapacitor; CP: compressor; PS: pumped storage; HPS: hydropower station; TESS: thermal energy storage system; WPS: wave power system; HLDR: hydrogen load demand response; HPR: hydrogen production rate; LPSP: loss of power supply probability; LCOH: levelized cost of hydrogen; LOEE: loss of energy expected; NPV: net present value; LCOE: levelized cost of energy; DNPV: daily net present value; AOP: annualized operating profits.

ing and representation of the system, failing to provide a dispatch strategy for the intraday phase of actual operations. Existing studies also overlook the balance between system benefits and individual electrolyzer stability, and separate supply-side and demand-side optimization. This study aims to address this gap by modeling HES under various scenarios of large-scale renewable energy generation and incorporating the proposed joint WT–PV power forecasting model and HL demand response (HLDR). Specifically, this study seeks to investigate how the optimization of scheduling strategies across multiple time scales can improve the operational characteristics and economics of HES under source–load uncertainty. The main contributions of this study are summarized as follows:

(1) A low-error joint WT–PV power prediction model is developed to accurately address the volatility of wind and PV power generation, demonstrating the model's validity and superiority. Additionally, a coupled HLDR model is innovatively constructed to fill the gap of separated supply–demand optimization. This approach comprehensively accounts for the impact of flexible HL on system sustainability, robustness, and economics.
(2) The HES modules are modeled in detail, with the operating characteristics of different electrolyzers represented by distinct state variables. Multiple constraints reflecting the actual operating conditions of the components are considered, and the Big-M method is applied to address nonlinear problems. A balance is achieved between model accuracy, engineering feasibility, and computational efficiency.
(3) A multi-timescale optimization scheduling strategy for HES is proposed, breaking the limitation of simple electrolyzer stacking in existing studies. It optimizes the system's energy flow scheduling to enhance the stable operation and efficient hydrogen production capacity of each electrolyzer while maximizing economic benefits.

This paper is structured as follows: Section 2 outlines the system structure and the modeling process of each model in HES; Section 3 details the optimization method, objective function, and constraints; Section 4 discusses the case setup and results; and Section 5 presents the conclusions.

2. Model description

2.1. System structure

In this study, the entire system consists of WT, PV, MG, ALK, PEM, battery, hydrogen storage tank (HST), and a voltage converter. The overall system structure is illustrated schematically in Fig. 1. The WT and PV continuously generate power, which is fed into the system as the power input. All the generated power is connected to the direct current (DC) bus, and most of the power in the DC bus is used for electrolysis consumption in the electrolyzer bank. The electrolyzer bank consists of ALKs and PEMs, integrated into multiple arrays to maximize hydrogen production under stable operation. This is achieved by coordinating the output time and variable load status of each electrolyzer. The generated hydrogen is distributed to the HL for on-demand sale via the HST. The HL in this study specifically targets flexible industrial and commercial users with adjustable hydrogen consumption behaviors. The HST also buffers the hydrogen flow to ensure a relatively stable hydrogen outflow. Additionally, the system is equipped with a battery to store and release power according to the system's power load and capacity, helping to alleviate load pressure. Simultaneously, the system is connected to the MG, which operates based on time-of-use pricing in the power market and the system's supply–demand balance. This facilitates the strategic purchase and sale of electricity, enhancing the system's economy and stability. Detailed modeling information for each device provided in Section S1 of Appendix A.

The entire REHPS is controlled and dispatched by the energy management system (EMS), which considers factors such as wind speed, solar irradiation intensity, and the operating status of each component to develop an optimal energy flow distribution strategy. The EMS then controls the DC bus by issuing scheduling instructions, and allocating the required power to each component based on the scheduling strategy. This ensures the stable operation of both the system and its components while enhancing economic efficiency and sustainability. Meanwhile, to ensure that the hydrogen produced meets the basic needs of the HL, the EMS provides instructions to the demand response (DR) system based on the

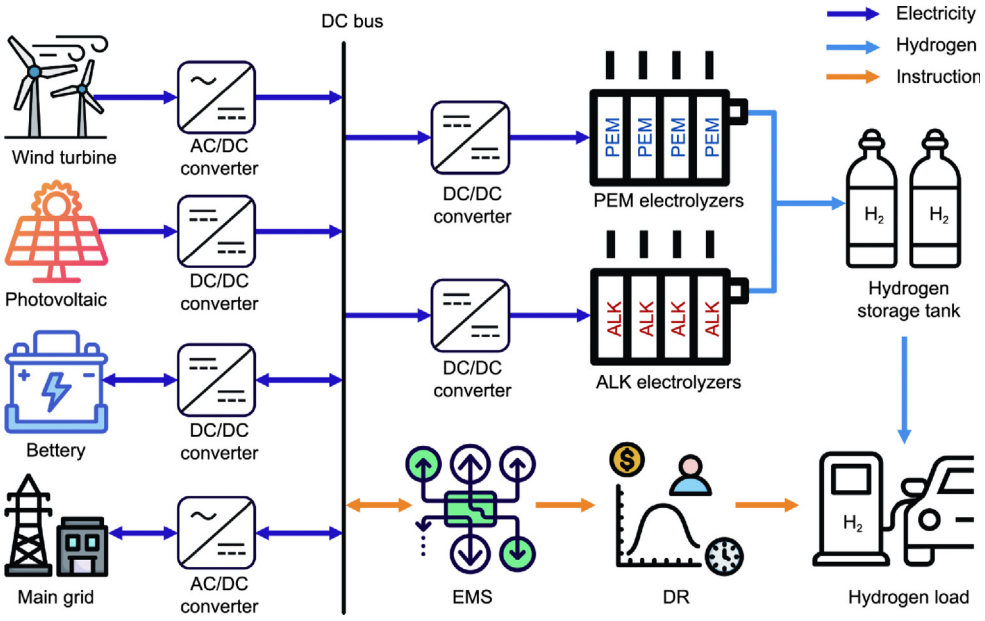

Fig. 1. System structure diagram of REHPS. AC: alternating current; EMS: energy management system; DR: demand response.

day's WT and PV power forecast. The DR system responds quickly, adjusting hydrogen prices and formulating incentive policies to influence user behavior. This, in turn, indirectly alters hydrogen demand, leading to time-varying HL.

2.2. DR model

This study investigates the impact of flexible hydrogen demand on the optimization of REHPS scheduling by constructing two types of DR models: price-based and incentive-based [31]. By innovatively extending the traditional electrical load demand response to the HL domain, this study demonstrates that HLDR is highly adaptable to hydrogen production systems.

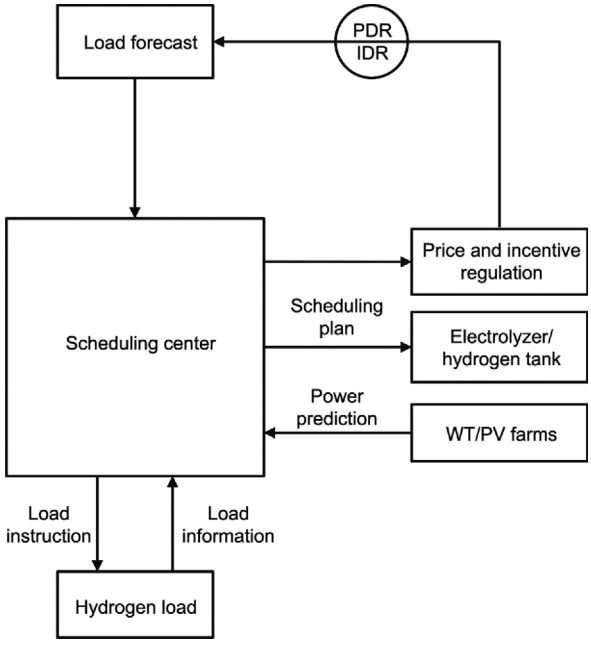

Fig. 2. Schematic diagram of HLDR. PDR: price-based DR; IDR: incentive-based DR.

The principle of HLDR in this study is illustrated in Fig. 2. The system scheduling center performs day-ahead load forecasting by gathering customer-side HL information. Simultaneously, the scheduling center receives the power forecast curves for wind and PV farms. The scheduling center combines load demand with wind and solar power output curves. It adjusts hydrogen prices accordingly—lowering them during peak generation and raising them during troughs. Additionally, targeted incentive policies are implemented to encourage the load side to purchase hydrogen when renewable energy is abundant and to decrease hydrogen demand during the trough of the wind power curve. After simulating the load response for peak shaving and valley filling, an updated load forecast is generated. The scheduling center schedules the electrolyzers, HST, and other components for the following day based on the updated load forecast curve. The load side also changes its energy use behavior for the next day based on the load instructions received.

2.2.1. Flexible HL

Loads are classified into four categories: fixed load (FL), shiftable load (SL), interruptible load (IL), and replaceable load (RL). This study focuses on evaluating the hydrogen production capacity of the HES, excluding the RL generated by horizontal substitution between hydrogen and other energy sources. The HL in this study specifically includes: flexible industrial users with batch production processes, which can shift hydrogen consumption time slots or temporarily reduce load by adjusting production schedules; hydrogen refueling stations with storage capacity, which can store hydrogen during low-price periods and use stored hydrogen during high-price periods. The actual HL (L^t_{act}) at any given time t consists of two components: the basic HL (L^t_{base}), which is required to meet the users' daily energy demand, and the extra HL (L^t_{extra}), which is influenced by various factors and generated based on the users' needs and system economic efficiency. Since L^t_{base} is solely determined by user demand, HLDR directly influences L^t_{base} in this study. Although the magnitude of L^t_{extra} is influenced by both supply and demand, its upper limit is typically determined by L^t_{base} alone, following a linear relationship. In summary, the flexible HL in this system can be expressed as follows:

$$L_{\text{base}}^{t} = \bar{L}_{\text{base}}^{t} + \Delta L_{\text{SL}}^{t} + \Delta L_{\text{IL}}^{t} \tag{1}$$

$$\begin{cases} L_{\text{act}}^{t} = L_{\text{base}}^{t} + L_{\text{extra}}^{t} \\ 0 \le L_{\text{extra}}^{t} \le \delta_{\text{L}} L_{\text{base}}^{t} \end{cases} \tag{2}$$

where $\bar{L}_{\text{base}}^{t}$ represents the base load at time t when there is no load variation; ΔL_{SL}^{t} and ΔL_{IL}^{t} denote the changes in the SL and IL, respectively, at time t; and δ_{L} represents the linear relationship between L_{extra}^{t} and L_{base}^{t}, as determined by the user.

2.2.2. Price-based DR

Hydrogen energy shares similar commodity properties with electricity. According to microeconomic theory, variations in energy prices influence changes in user energy consumption [32]. In this study, price-based DR (PDR) is implemented to establish time-of-use hydrogen prices, influenced by the day-ahead wind and PV power forecasts. The adjustment factor is the ratio of the average total input power at each moment of the day-ahead to the actual output power at that moment. Its calculation is given by the following equation:

$$p^{t} = \delta_{\text{H}_2} \bar{p}^{t} \tag{3}$$

$$\begin{cases} \delta_{\text{H}_2} = \dfrac{\frac{1}{T}\sum_{i=1}^{T}\left(P_{\text{WT}}^{t} + P_{\text{PV}}^{t}\right)}{P_{\text{WT}}^{t} + P_{\text{PV}}^{t}} \\ \delta_{\min}^{\text{H}_2} \le \delta_{\text{H}_2} \le \delta_{\max}^{\text{H}_2} \end{cases} \tag{4}$$

where p^{t} and $\bar{p}^{t}$ represent the hydrogen price at time t after and before the price change, respectively; δ_{H_2} is the hydrogen price adjustment factor; P_{WT}^{t} and P_{PV}^{t} represent the power of WT and PV at time t, respectively; T is the day-ahead scheduling period, assumed to be 24 h; and $\delta_{\min}^{\text{H}_2}$ and $\delta_{\max}^{\text{H}_2}$ represent the minimum and maximum values of the adjustment factor, respectively.

By calculating the ratio of the hydrogen energy price to the corresponding change, a price elasticity matrix can be created, which includes both own-price and cross-price elasticity coefficients [33]. Detailed data sources and parameter configuration methods for the matrix are provided in Section S2 of Appendix A.

$$\boldsymbol{M_0} = \begin{bmatrix} m^{11} & m^{12} & \cdots & m^{1v} \\ m^{21} & m^{22} & \cdots & m^{2v} \\ \vdots & \vdots & \ddots & \vdots \\ m^{u1} & m^{u2} & \cdots & m^{uv} \end{bmatrix} \tag{5}$$

$$m^{uu} = \frac{\Delta L_{\text{PDR}}^{u}}{\bar{L}_{\text{PDR}}^{u}} \left(\frac{p^{u} - \bar{p}^{u}}{p^{u}} \right)^{-1} \tag{6}$$

$$m^{uv} = \frac{\Delta L_{\text{PDR}}^{u}}{\bar{L}_{\text{PDR}}^{u}} \left(\frac{p^{v} - \bar{p}^{v}}{p^{v}} \right)^{-1} \tag{7}$$

where $\boldsymbol{M_0}$ is the hydrogen price elasticity matrix; u and v denote the moment in time; m^{uu} is the own-price elasticity coefficient; m^{uv} represents the cross-price elasticity coefficient; $\bar{L}_{\text{PDR}}^{u}$ is the load demand without PDR at moment u; L_{PDR}^{u} is the load demand with PDR at moment u, and $\Delta L_{\text{PDR}}^{u}$ is the load change with PDR at moment u.

In this study, PDR mainly involves SL, and SL refers to the vertical transfer and adjustment of load by users over a specific time period in response to energy price changes [34]. By properly scheduling SL, load fluctuations on the hydrogen side can be effectively smoothed, thus improving system stability. In this study, the operating time of SL is coordinated with renewable energy generation to maximize the use of renewable energy. The response model for SL is shown as [34]:

$$L_{\text{PDR}}^{t} = \bar{L}_{\text{PDR}}^{t} + \Delta L_{\text{SL}}^{t} \tag{8}$$

$$\Delta L_{\text{SL}}^{t} = \bar{L}_{\text{PDR}}^{t} \sum_{t=1}^{T} \left[\boldsymbol{M}_0(t,t') \cdot \left(p^{t'} - \bar{p}^{t'} \right) / \bar{p}^{t'} \right] \tag{9}$$

where ΔL_{SL}^{t} is the change in SL with PDR at time t.

2.2.3. Incentive-based DR

The method of altering load-side energy use behavior through appropriate incentive policies is called incentive-based DR (IDR). This study focuses on ILs in the context of IDR. IL allows users to respond to the incentive policy by reducing part of the load within a specified range based on their individual circumstances. The response model for IL is formulated as:

$$L_{\text{IDR}}^{t} = \bar{L}_{\text{IDR}}^{t} + \Delta L_{\text{IL}}^{\text{t}} \tag{10}$$

where L_{IDR}^{t} and $\bar{L}_{\text{IDR}}^{t}$ represent the load demand at time t with and without IDR, respectively; $\Delta L_{\text{IL}}^{\text{t}}$ is the change in IL at time t with IDR.

2.3. Joint WT–PV forecasting model

2.3.1. Forecasting model description

This study proposes a joint WT–PV power prediction model designed to accurately reflect the variation in renewable energy output. The model combines convolutional neural network (CNN), bidirectional long short-term memory neural network (BiLSTM), and Attention mechanism. CNN extracts data features, BiLSTM captures long-term relationships in the time series, and Attention enhances the model's ability to focus on key information in the input data. The model strikes a balance between prediction accuracy and computational efficiency, making it suitable for use in renewable energy hybrid hydrogen production systems. The framework of the model is shown in Fig. 3, and the main modeling steps are outlined below:

Step 1. The local meteorological data and historical wind power data are cleaned, with erroneous data removed and missing values filled in. The data are then analyzed for correlation to visualize the relationship between the two variables. The sample data are selected based on the Pearson correlation coefficient (PCC) to reduce redundancy and improve the quality of the input data. The sample data are then normalized to ensure consistency in variable dimensions and enhance the reliability of the predictive model. The data are then partitioned into a training set, validation set, and test set.

Step 2. Model training is conducted using the training set to design the joint WT–PV prediction model (CNN–BiLSTM–Attention). The input data (WT and PV) are passed through the CNN layer for feature extraction. The data then passes through the BiLSTM layer and into the dropout layer for regularization, which prevents overfitting and improves the model's generalization ability. The data is then processed by the Attention layer to capture key information, followed by the fully connected layer. Finally, the power data is output once the set number of iterations is reached.

Step 3. Cross-validation is performed on the data based on the training results to evaluate and improve the model's generalization ability. If the output requirements are not met, the model parameters are adjusted and retrained until the results satisfy the requirements, after which the model is used for prediction.

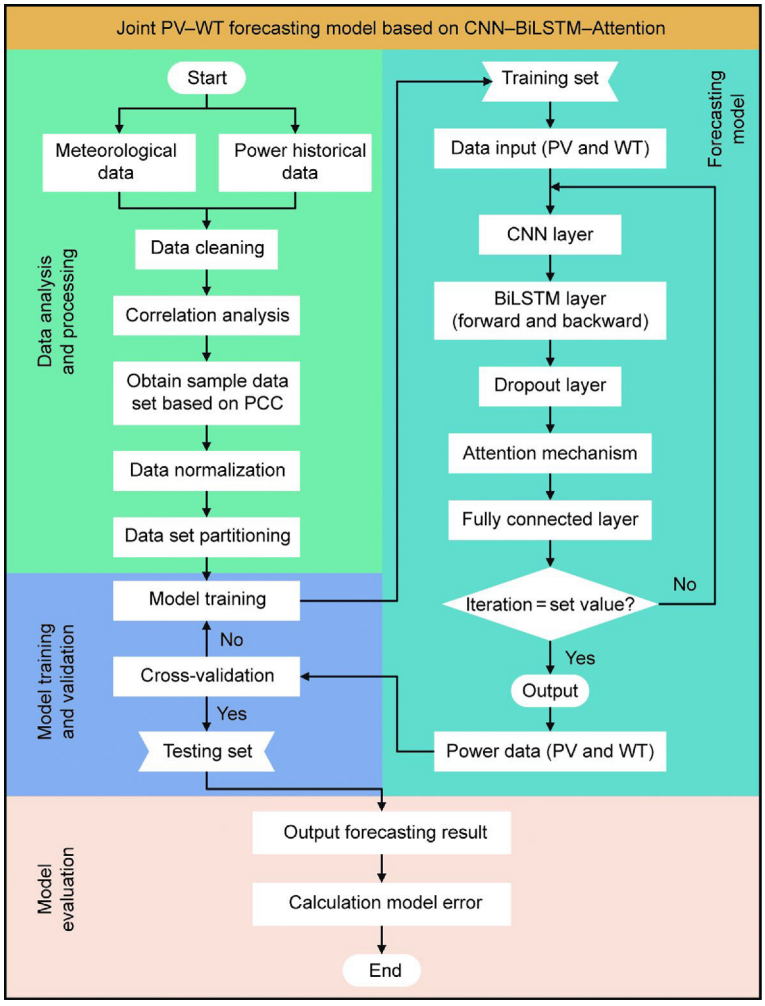

Fig. 3. Process framework for forecasting model. PCC: Pearson correlation coefficient.

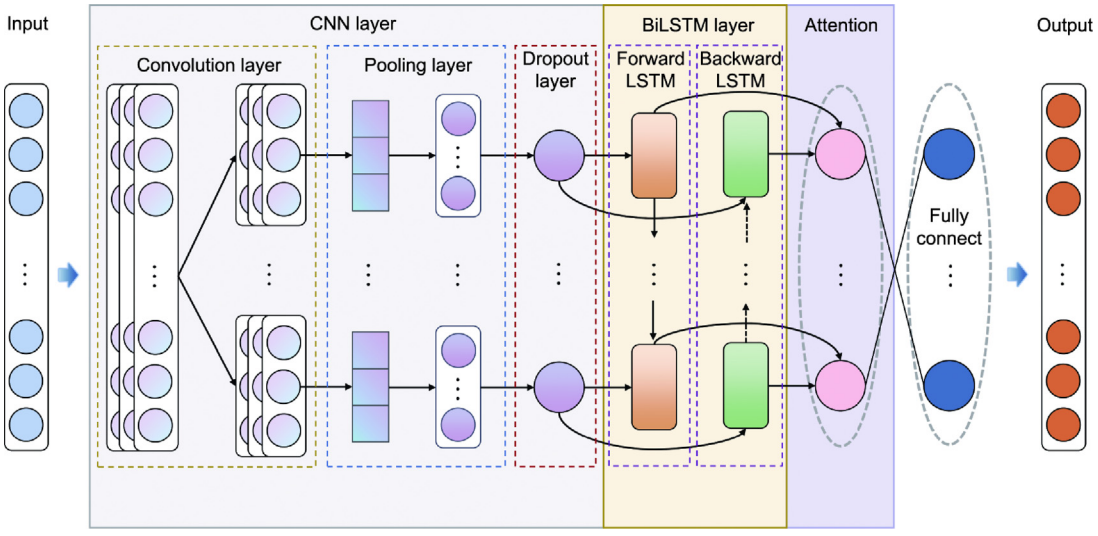

Fig. 4. Structure diagram of CNN–BiLSTM–Attention.

Step 4. Finally, the model prediction error is calculated using multiple evaluation metrics to validate and assess the model's effectiveness for comprehensive analysis.

2.3.2. CNN–BiLSTM–Attention model

The specific structure of the CNN–BiLSTM–Attention model for joint WT–PV prediction is shown in Fig. 4. The model connects

the CNN, BiLSTM, Attention mechanism, and fully connected layers in series, accurately capturing local features and long-term dependencies while maintaining computational efficiency and model accuracy. Detailed modeling, functional characterization, and schematic information for each unit are provided in Section S3 of Appendix A.

3. Methodology

A multi-timescale optimization strategy is proposed to optimize the entire system, based on the previous introduction of each model component. The flow of the proposed method is illustrated in Fig. 5. In this method, the HL elasticity matrix is established to respond to WT and PV power variations, ensuring HL demand and maximum production. PDR and IDR are adjusted based on the time-scaled hydrogen price. To address the inaccuracy of point prediction, which can lead to discrepancies between actual operation results and expected goals, a multi-timescale scheduling optimization strategy is introduced [35]. It consists of two parts: day-ahead scheduling and intraday scheduling. The day-ahead and intraday scheduling use power data from the corresponding time scales of wind and PV forecasts as inputs. By combining objective functions and constraints at different time scales, the intraday rolling optimization refines the day-ahead schedule and outputs the optimal results.

3.1. Rolling optimization strategy

The core of the multi-timescale optimization strategy is rolling optimization. Rolling optimization is an online process controlled by a fixed time window, with updates and repetitions occurring continuously. In this study, the day-ahead scheduling cycle is divided into 24 equal time steps, each with a 1-h time scale. The intraday scheduling cycle is divided into 96 equal time steps, each with a 15-min time scale. The intraday control period is 4 h, with operations rolling backward in 15-min intervals.

The principle of rolling optimization is to use the day-ahead optimization results as the initial schedule, with the intraday phase adjusting this plan. Each intraday optimization targets one control time domain, and only the result of the first time step in the domain is retained. The system then feeds back this optimization result and updates the component outputs. The system then moves one time step backward, using the optimization result as the initial variable for the next control domain. The optimization rolls forward and is fed back until all solutions for the day's schedule are completed. The specific optimization schematic is illustrated in Fig. 6.

3.2. Day-ahead objective function

This study aims to determine the optimal operating strategy for HES's stable operation and maximum economic benefits within a day. The optimal scheduling scheme for each system component is derived by balancing hydrogen sales gains with the economic losses from system operation. To prevent performance degradation due to frequent startups and shutdowns of the hybrid electrolyzers, the total number of switches is penalized in the objective function. The day-ahead optimization objective is to maximize total daily net revenue (C_{TR}), with the specific objective function including daily hydrogen sales revenue (C_{HR}), daily electricity trading revenue (C_{ER}), daily operation and maintenance costs (C_{OM}), daily equivalent investment costs (C_{INV}), electrolyzers' switching penalty

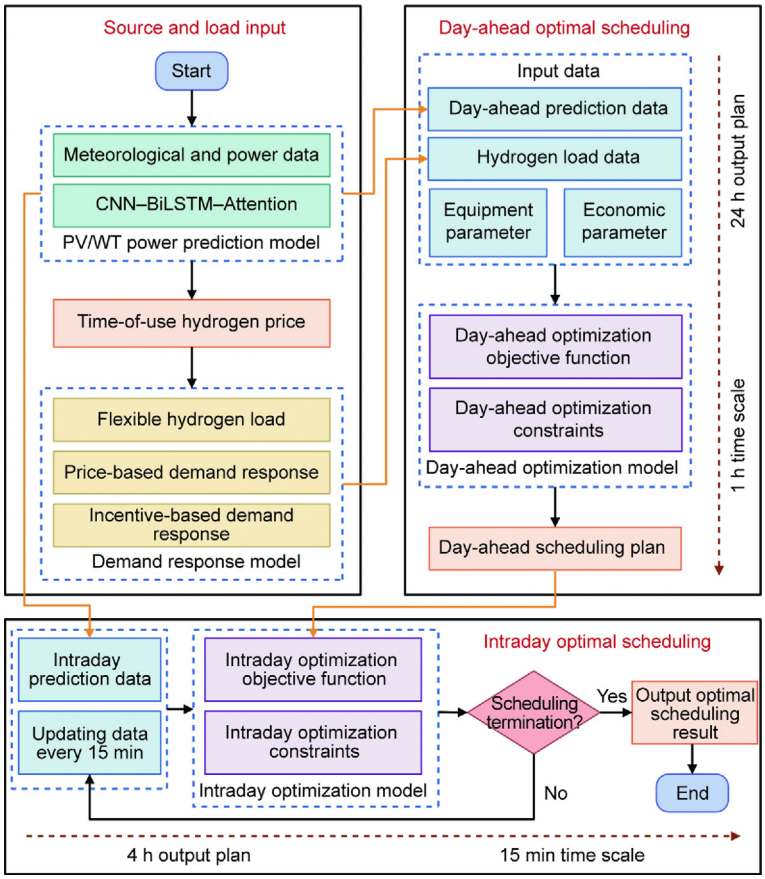

Fig. 5. Flowchart for multi-timescale optimization.

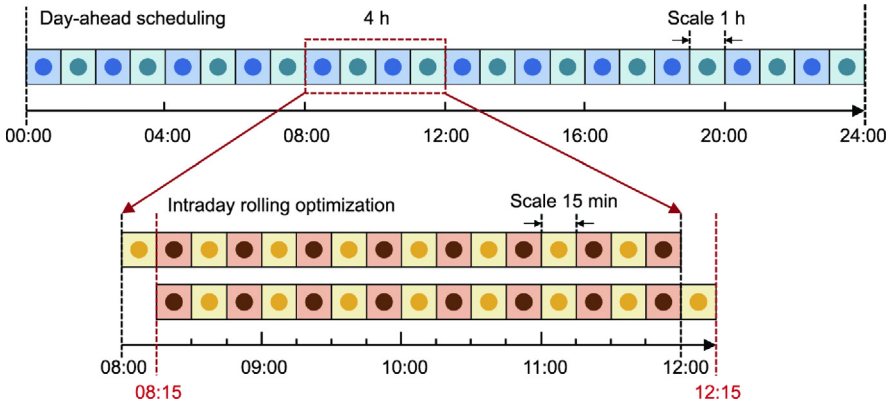

Fig. 6. Schematic diagram of rolling optimization.

(C_{SW}), incentive user costs (C_{IDR}), and labor costs (C_{Labor}). C_{TR} is formulated as:

$$\max C_{TR} = C_{HR} + C_{ER} - C_{OM} - C_{INV} - C_{SW} - C_{IDR} - C_{Labor} \tag{11}$$

In the objective function, the revenue consists of hydrogen sales revenue (C_{HR}) and electricity trading revenue (C_{ER}). C_{HR} represents the hydrogen generated from ALK and PEM electrolysis, which is stored in the HST. The hydrogen is then withdrawn from the HST and sold based on the actual HL (L^t_{act}). The basic HL (L^t_{base}) is sold at the time-of-day hydrogen price after applying DR, while the extra load (L^t_{extra}) is sold at the original market hydrogen price. C_{ER} is the revenue from power trading, which the system conducts to ensure the stability of the power supply. The system also attempts to make a profit by selling electricity at peak prices and purchasing at low prices. The revenue is described as:

$$C_{HR} = \sum_{t=1}^{T} \left(p^t_{H_2} L^t_{base} + p^o_{H_2} L^t_{extra} \right) \tag{12}$$

$$C_{ER} = \sum_{t=1}^{T} \left(p^t_s P^t_s - p^t_b P^t_b \right) \tag{13}$$

where $p^t_{H_2}$ is the hydrogen price after applying DR at time t; $p^o_{H_2}$ is the original market hydrogen price; p^t_s and p^t_b are the selling and purchasing prices of electricity in the power market at time t, respectively; and P^t_s and P^t_b represent the electricity sold and purchased by the system in its transaction with the grid at time t, respectively.

The operation and maintenance cost (C_{OM}), daily equivalent investment cost (C_{INV}), and penalty cost (C_{SW}) for frequent startup/shutdown of the electrolyzers are the primary considerations for operation and economic loss. C_{OM} is determined by the unit operation and maintenance cost of each component and its output power; C_{INV} is determined by the unit assembly cost, design life, and configured capacity of each component; and C_{SW} primarily concerns the frequency of ALK startup and shutdown as a penalty cost due to the fast response capability of PEM. The equipment aging cost of the electrolyzer is included in both the operation and maintenance cost and the start–stop penalty cost. Since this study focuses on exploring the economic benefits within a single day, it does not address replacement costs after the equipment reaches its design life. Instead, the capital recovery rate over each component's design life is calculated to determine the corresponding investment cost. From the above analysis, it is clear that the economic loss cost of each component is closely related to the type of equipment. The specific calculation of this economic loss is as follows [22]:

$$\begin{cases} C_{OM} = \sum_{i \in X} \left(\sum_{t=1}^{T} C_{OM,i} P^t_i \right) + C_{H_2O} \\ C_{H_2O} = \sum_{t=1}^{T} \left(p_{H_2O} m^t_{H_2O} \right) \\ X = \{WT,\ PV,\ BAT,\ ALK_j,\ PEM_k,\ HST\} \end{cases} \tag{14}$$

$$\begin{cases} C_{INV} = \sum\limits_{i \in X} \mu_{C,i} C_{INV,i} S_i \\ \mu_{C,i} = \left(\frac{b(1+b)^{LP_i}}{(1+b)^{LP_i}-1} \right) / n^a \\ X = \{WT,\ PV,\ BAT,\ ALK_j,\ PEM_k,\ HST\} \end{cases} \tag{15}$$

$$C_{SW} = C_{Y_{ALK}} N_{SW} \tag{16}$$

where $C_{OM,i}$ denotes the unit operation and maintenance cost of equipment i; Q denotes the operation power of equipment i at time t; X is the set of equipment types; j and k denote different ALKs and PEMs, respectively($j \in n_{ALK}$, $k \in n_{PEM}$); n_{ALK} and n_{PEM} denote the quantities of ALKs and PEMs, respectively; C_{H_2O} denotes the cost of water used in hydrogen production; p_{H_2O} denotes the price of water; $m^t_{H_2O}$ denotes the total water consumed by the electrolyzer at time t; $C_{INV,i}$ denotes the unit assembly cost of equipment i; S_i denotes the configured capacity of equipment i; $\mu_{C,i}$ denotes the capital payback rate of equipment i; b denotes the social discount rate; LP_i denotes the design service life of equipment i; n^a denotes the operating cycle of the entire system; $C_{Y_{ALK}}$ denotes the ALK cold start-up penalty coefficient; and N_{SW} denotes the total number of switches of all electrolyzers.

3.3. Day-ahead constraints

In REHPS, fine-grained constraints must be imposed on key equipment such as electrolyzers to ensure the stable and effective operation of the system. The constraints on the operation of key components are described in detail below.

3.3.1. Hybrid electrolyzers constraints

Most existing studies only model basic on/off states of a single-category electrolyzer, leading to inaccurate modeling. To fill this gap, this study considers the different operating states of each electrolyzer to refine the operating states of ALK and PEM, leveraging their respective state characteristics in HES. Transitions between different operating states will also have varying operating modes. Restarting a hydrogen plant after a complete shutdown is called a cold start. In cold start mode, the electrolyzer starts at a lower temperature and gradually warms up to its operating temperature before entering the hydrogen production state. To prevent frequent startups and shutdowns that could reduce system efficiency, the electrolyzer can be run in standby mode for subsequent startups,

if necessary. The standby power of the electrolyzer is typically 5% of the rated power, maintaining the operating temperature without producing hydrogen. Restarting hydrogen production from standby is called a hot start. Hot start is typically used for shorter shutdowns and is much faster than cold start. Additionally, PEM can briefly exceed its rated power (≤ 120%) to operate in an overloaded condition for hydrogen production [5]. From the analysis, it is clear that ALK operates in three modes: hydrogen production, standby, and shutdown due to its slower responsiveness and need to operate at rated power; PEM operates in three states: overload, hydrogen production, and shutdown due to its faster start/stop capability and broader load characteristics. The specific transition process for each operation state is shown in Fig. 7, with each state represented by a binary variable:

$$L_{\mathrm{ALK}}^{t}+S_{\mathrm{ALK}}^{t}+I_{\mathrm{ALK}}^{t}=1 \tag{17}$$

$$R_{\mathrm{PEM}}^{t}+L_{\mathrm{PEM}}^{t}+I_{\mathrm{PEM}}^{t}=1 \tag{18}$$

where L_{ALK}^{t}, S_{ALK}^{t}, and I_{ALK}^{t} as binary variables, denote the ALK states of hydrogen production, standby, or shutdown at time t; R_{PEM}^{t}, L_{PEM}^{t}, and I_{PEM}^{t} denote the PEM states of overload, hydrogen production, or shutdown at time t, respectively.

(1) Cold/hot start-up constraints. This study focuses on cold/hot start constraints for ALK, where binary variables Y_{ALK}^{t} and W_{ALK}^{t} are used to represent whether ALK is in cold start or hot start mode at time t. These are solved by constructing the following mixed integer linear programming (MILP) equations [36]:

$$\begin{cases} Y_{\mathrm{ALK}}^{t}\le I_{\mathrm{ALK}}^{t} \\ Y_{\mathrm{ALK}}^{t}\le S_{\mathrm{ALK}}^{t+1}+L_{\mathrm{ALK}}^{t+1} \\ Y_{\mathrm{ALK}}^{t}\ge S_{\mathrm{ALK}}^{t+1}+L_{\mathrm{ALK}}^{t+1}+I_{\mathrm{ALK}}^{t}-1 \end{cases} \tag{19}$$

$$\begin{cases} W_{\mathrm{ALK}}^{t}\le S_{\mathrm{ALK}}^{t} \\ W_{\mathrm{ALK}}^{t}\le L_{\mathrm{ALK}}^{t+1} \\ W_{\mathrm{ALK}}^{t}\ge S_{\mathrm{ALK}}^{t}+L_{\mathrm{ALK}}^{t+1}-1 \end{cases} \tag{20}$$

(2) Load variation constraints. To avoid frequent startup/shutdown of the electrolyzer in a short period, it is necessary to limit the minimum downtime and minimum operating time. The maximum overload time constraint must also be considered for the PEM, as prolonged overload can shorten its lifespan. These three items are formulated as:

$$\begin{cases} \sum_{\tau=t}^{t+T_{\min}^{\mathrm{I},x}-1} I_{x}^{\tau}\ge T_{\min}^{\mathrm{I},x}\left(I_{x}^{t}-I_{x}^{t-1}\right) \\ \sum_{\tau=t}^{t+T_{\min}^{\mathrm{S},x}-1} S_{x}^{\tau}\ge T_{\min}^{\mathrm{S},x}\left(S_{x}^{t}-S_{x}^{t-1}\right) \\ \sum_{\tau=t}^{t+T_{\max}^{\mathrm{R,PEM}}-1} R_{\mathrm{PEM}}^{\tau}\le T_{\max}^{\mathrm{R,PEM}}\left(R_{\mathrm{PEM}}^{t}-R_{\mathrm{PEM}}^{t-1}\right) \end{cases} \tag{21}$$

where $T_{\min}^{\mathrm{I},x}$ and $T_{\min}^{\mathrm{S},x}$ denote the minimum downtime and minimum operating time, respectively; x refers to either ALK or PEM; and $T_{\max}^{\mathrm{R,PEM}}$ denotes the maximum overload time for PEM.

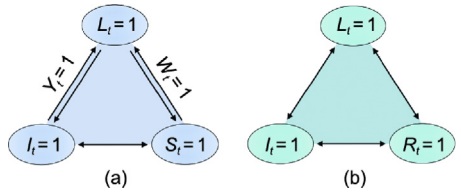

Fig. 7. Operation states of (a) ALK and (b) PEM. I_t: shutdown; S_t: standby; L_t: hydrogen production; R_t: overload; Y_t: cold start; W_t: hot start.

Prolonged operation of the electrolyzer at low power may cause gas crossover in the tank, posing risks such as hydrogen explosion [30]. As a result, the variable load range of ALK and PEM is limited to:

$$0.05S_{\mathrm{ALK}}^{t}P_{\max}^{\mathrm{ALK}}+L_{\mathrm{ALK}}^{t}P_{\min}^{\mathrm{ALK}}\le P_{\mathrm{ALK}}^{t}\le 0.05S_{\mathrm{ALK}}^{t}P_{\max}^{\mathrm{ALK}}+L_{\mathrm{ALK}}^{t}P_{\max}^{\mathrm{ALK}} \tag{22}$$

$$L_{\mathrm{PEM}}^{t}P_{\min}^{\mathrm{PEM}}+R_{\mathrm{PEM}}^{t}P_{\max}^{\mathrm{PEM}}\le P_{\mathrm{PEM}}^{t}\le L_{\mathrm{PEM}}^{t}P_{\max}^{\mathrm{PEM}}+1.2R_{\mathrm{PEM}}^{t}P_{\max}^{\mathrm{PEM}} \tag{23}$$

where P_{ALK}^{t} and P_{PEM}^{t} denote the operating power of ALK and PEM at time t, respectively; $P_{\min}^{\mathrm{ALK}}$ and $P_{\max}^{\mathrm{ALK}}$ represent the minimum limiting power and rated power of ALK; and $P_{\min}^{\mathrm{PEM}}$ and $P_{\max}^{\mathrm{PEM}}$ denote the minimum limiting power and rated power of PEM, respectively.

(3) Hydrogen production constraints. During the cold or hot start-up of the ALK, power fluctuations can lead to gas crossover, causing the hydrogen purity to fall below the production quality standard. To accurately characterize high-quality hydrogen production over time, the hydrogen loss during the ALK startup process must be considered. In this study, assuming that the power during the startup process is used solely to feed the system without producing hydrogen, the actual hydrogen production rate per ALK is calculated as [25]:

$$\lambda_{\mathrm{Y,ALK}}=1-T_{\mathrm{Y,ALK}}/60,\lambda_{\mathrm{W,ALK}}=1-T_{\mathrm{W,ALK}}/60 \tag{24}$$

$$m_{\mathrm{H_2,ALK}}^{t}=\eta_{\mathrm{ALK}}\left(L_{\mathrm{ALK}}^{t}+\lambda_{\mathrm{Y,ALK}}Y_{\mathrm{ALK}}^{t}+\lambda_{\mathrm{W,ALK}}W_{\mathrm{ALK}}^{t}\right)P_{\mathrm{ALK}}^{t}/\xi_{\mathrm{ALK}} \tag{25}$$

where $\lambda_{\mathrm{Y,ALK}}$ and $\lambda_{\mathrm{W,ALK}}$ represent the hydrogen production correction factors for cold and hot starts, respectively; $T_{\mathrm{Y,ALK}}$ and $T_{\mathrm{W,ALK}}$ denote the durations (unit: min) of the cold and hot starts of the ALK, respectively; $m_{\mathrm{H_2,ALK}}^{t}$ represents the mass of hydrogen produced by the ALK at time t; η_{ALK} is the hydrogen production efficiency of the ALK; and ξ_{ALK} denotes the electricity consumption per unit of hydrogen produced.

The constraints above transform the problem into a mixed integer nonlinear programming (MINLP) problem, complicating the solution process and reducing computational efficiency. On the other hand, existing studies overlook hydrogen losses during the electrolyzer startup phase, failing to comprehensively simulate hydrogen production yields. To address these, the study employs the Big-M linear programming method to linearize the nonlinear problem [37]. This method replaces the original nonlinear terms with linear constraints by introducing additional variables and a large constant M. Simultaneously, it precisely simulates each state transition process to ensure that the optimal solution remains unchanged before and after the transformation [38]. The specific modified equation is formulated as:

$$\begin{cases} P_{\mathrm{L,ALK}}^{t}\le P_{t}^{\mathrm{AEL}},P_{\mathrm{L,ALK}}^{t}\le L_{\mathrm{ALK}}^{t}\mathrm{M},P_{\mathrm{L,ALK}}^{t}\ge P_{\mathrm{ALK}}^{t}-\left(1-L_{\mathrm{ALK}}^{t}\right)\mathrm{M} \\ P_{\mathrm{Y,ALK}}^{t}\le\lambda_{\mathrm{Y,ALK}}P_{\mathrm{ALK}}^{t},P_{\mathrm{Y,ALK}}^{t}\le Y_{\mathrm{ALK}}^{t}\mathrm{M},P_{\mathrm{Y,ALK}}^{t}\ge\lambda_{\mathrm{Y,ALK}}P_{\mathrm{ALK}}^{t}-\left(1-Y_{\mathrm{ALK}}^{t}\right)\mathrm{M} \\ P_{\mathrm{W,ALK}}^{t}\le\lambda_{\mathrm{W,ALK}}P_{\mathrm{ALK}}^{t},P_{\mathrm{W,ALK}}^{t}\le W_{\mathrm{ALK}}^{t}\mathrm{M},P_{\mathrm{W,ALK}}^{t}\ge\lambda_{\mathrm{W,ALK}}P_{\mathrm{ALK}}^{t}-\left(1-W_{\mathrm{ALK}}^{t}\right)\mathrm{M} \\ P_{\mathrm{Y,ALK}}^{t}\ge 0,P_{\mathrm{W,ALK}}^{t}\ge 0,P_{\mathrm{L,ALK}}^{t}\ge 0 \\ m_{\mathrm{H_2,ALK}}^{t}=\eta_{\mathrm{ALK}}\left(P_{\mathrm{L,ALK}}^{t}+P_{\mathrm{Y,ALK}}^{t}+P_{\mathrm{W,ALK}}^{t}\right)/\xi_{\mathrm{ALK}} \end{cases} \tag{26}$$

where $P_{\mathrm{L,ALK}}^{t}$, $P_{\mathrm{Y,ALK}}^{t}$, and $P_{\mathrm{W,ALK}}^{t}$ represent the actual effective hydrogen production power of the ALK during hydrogen production, cold start, and hot start, respectively. Since these are in different states, only one can be non-zero at any given moment.Finally, by combining the hydrogen production equations of ALK and PEM, the total hydrogen production rate of the hybrid hydrogen system, as well as the mass flow rate into the HST, denoted as $m_{\mathrm{HST,in}}^{t}$, is obtained as:

$$\begin{cases} m^t_{\mathrm{HST,in}} = \sum_{j=1}^{n_{\mathrm{ALK}}} m^t_{\mathrm{H_2,ALK}_j} + \sum_{k=1}^{n_{\mathrm{PEM}}} m^t_{\mathrm{H_2,PEM}_k} \\ m^t_{\mathrm{H_2,PEM}} = \eta_{\mathrm{PEM}} P^t_{\mathrm{PEM}} / \xi_{\mathrm{PEM}} \end{cases} \tag{27}$$

This yields the water consumption rate of the HES, denoted as $m^t_{\mathrm{H_2O}}$:

$$m^t_{\mathrm{H_2O}} = m^t_{\mathrm{HST,in}} M_{\mathrm{H_2O}} / M_{\mathrm{H_2}} \tag{28}$$

where $M_{\mathrm{H_2O}}$ and $M_{\mathrm{H_2}}$ denote the relative molecular masses of H_2O and H_2, respectively.

3.3.2. Battery and hydrogen storage constraints

$$\begin{cases} P^{\mathrm{BAT}}_{\min} \le P^t_{\mathrm{BAT,ch}} \le P^{\mathrm{BAT}}_{\max} \\ P^{\mathrm{BAT}}_{\min} \le P^t_{\mathrm{BAT,dis}} \le P^{\mathrm{BAT}}_{\max} \\ \mathrm{SOC}_{\min} \le \mathrm{SOC}_t \le \mathrm{SOC}_{\max} \\ \mathrm{SOC}_0 = \mathrm{SOC}_{\mathrm{end}} \end{cases} \tag{29}$$

where $P^t_{\mathrm{BAT,ch}}$ and $P^t_{\mathrm{BAT,dis}}$ denote the battery charging and discharging powers (at the DC bus level) at time t, respectively; $P^{\mathrm{BAT}}_{\min}$ and $P^{\mathrm{BAT}}_{\max}$ denote the minimum and maximum charging and discharging power of the battery, respectively; $\mathrm{SOC}_{\min}$ and $\mathrm{SOC}_{\max}$ represent the minimum and maximum state of charge of the battery; while SOC_0 and $\mathrm{SOC}_{\mathrm{end}}$ denote the initial and end values of the state of charge for the day, typically set to 0.5, used to maintain charge stability at the start and end of the day. The same applies to the HST:

$$\begin{cases} 0 \le m^t_{\mathrm{HST,in}} \le m^{\mathrm{HST}}_{\max} \\ 0 \le m^t_{\mathrm{HST,out}} \le m^{\mathrm{HST}}_{\max} \\ \mathrm{LOH}_{\min} \le \mathrm{LOH}_t \le \mathrm{LOH}_{\max} \\ \mathrm{LOH}_0 = \mathrm{LOH}_{\mathrm{end}} \end{cases} \tag{30}$$

where $m^t_{\mathrm{HST,in}}$ and $m^t_{\mathrm{HST,out}}$ denote the inlet and outlet hydrogen mass flow rates of the HST at time t, respectively; $m^{\mathrm{HST}}_{\max}$ denotes the maximum mass flow rate at the hydrogen inlet and outlet of the HST; $\mathrm{LOH}_{\min}$ and $\mathrm{LOH}_{\max}$ represent the minimum and maximum load factor of the HST; while LOH_0 and $\mathrm{LOH}_{\mathrm{end}}$ denote the initial and end values of the load factor for the day, typically set to 0.5, used to maintain the stability of the HST's operation at the start and end of the day.

3.3.3. Electricity trading constraints

The power traded to the larger grid must be controlled within the upper power limit of the contact line ($P^{\mathrm{MG}}_{\max}$):

$$\begin{cases} 0 \le P^t_{\mathrm{b}} \le P^{\mathrm{MG}}_{\max} \\ 0 \le P^t_{\mathrm{s}} \le P^{\mathrm{MG}}_{\max} \end{cases} \tag{31}$$

3.3.4. Electricity and hydrogen balance constraints

At any moment, the input and output power of the DC bus must be balanced to maintain system stability:

$$P^t_{\mathrm{WT}} + P^t_{\mathrm{PV}} + P^t_{\mathrm{BAT,dis}} + P^t_{\mathrm{b}} = \sum_{j=1}^{n_{\mathrm{ALK}}} P^t_{\mathrm{ALK}_j} + \sum_{k=1}^{n_{\mathrm{PEM}}} P^t_{\mathrm{PEM}_k} + P^t_{\mathrm{BAT,ch}} + P^t_{\mathrm{s}} \tag{32}$$

Similarly, the balance of hydrogen inflow and outflow in the HST is required to maintain the stability of hydrogen supply and demand:

$$E^t_{\mathrm{HST}} = E^{t-1}_{\mathrm{HST}} + \left(m^t_{\mathrm{HST,in}} - m^t_{\mathrm{HST,out}} \right) \Delta t \tag{33}$$

where E^t_{HST} is the remaining capacity of the HST at time t.

3.3.5. DR constraints

Depending on actual demand, the shiftable and ILs must be controlled within the maximum variations $\Delta L^{\mathrm{SL}}_{\max}$ and $\Delta L^{\mathrm{IL}}_{\max}$:

$$\begin{cases} 0 \le \Delta L^t_{\mathrm{SL}} \le \Delta L^{\mathrm{SL}}_{\max} \\ 0 \le \Delta L^t_{\mathrm{IL}} \le \Delta L^{\mathrm{IL}}_{\max} \end{cases} \tag{34}$$

3.4. Intraday objective function

The core of intraday optimization is rolling optimization, which aims to minimize deviations in equipment power output from the day-ahead scheduling plan. Existing intraday strategies focus solely on economic efficiency while neglecting equipment stability. In the hybrid hydrogen production system of this study, maintaining stable power output for each ALK and PEM (both key energy-consuming components for renewable energy) is especially critical. Thus, we minimize deviations from the day-ahead plan to ensure stable operation of each electrolyzer. Simultaneously, the battery and power trading systems must minimize power output deviations while performing peak shaving and valley filling for the system. Consequently, the adjustment of each piece of equipment is formulated as a penalty function, with the intraday optimization objective being to minimize the sum of these adjustments compared to the previous day's plan. The total penalty (C_{TP}) is calculated as:

$$\begin{cases} \min C_{\mathrm{TP}} = \sum_{i \in X} \left[\mu_i \sum_{t=1}^{T} \left(P^t_i - P^t_{i,0} \right) \right] + \mu_{\mathrm{SW}} C_{\mathrm{SW}} \\ X = \left\{ \mathrm{ALK}_j,\ \mathrm{PEM}_k,\ \mathrm{BAT_{ch}},\ \mathrm{BAT_{dis}},\ \mathrm{MG_{buy}},\ \mathrm{MG_{sell}} \right\} \end{cases} \tag{35}$$

where P^t_i and $P^t_{i,0}$ represent the day-ahead output plan and intraday output of equipment i, respectively; μ_i is the penalty adjustment compensation factor for equipment i; and μ_{SW} is the electrolyzer start–stop penalty compensation factor.

Quantifying the effectiveness of the intraday optimization strategy in tracking the day-ahead plan is essential. The execution rate is defined as the overall average of power deviations across all components at each time step. This metric effectively reflects the system's adherence to the day-ahead plan. Mathematically, it is calculated as follows:

$$\text{Execution Rate} = \left[\frac{1}{T \times |X|} \sum_{i \in X} \sum_{t=1}^{T} \left(1 - \frac{\left| P^t_i - P^t_{i,0} \right|}{P^t_{i,0}} \right) \right] \times 100\% \tag{36}$$

where $|X|$ represents the total number of components included in the set X. Therefore, in this model, $|X|$ is set to 6.

3.5. Intraday constraints

The intraday scheduling phase is optimized on a rolling 15-min scale; therefore, the constraints must include Eqs. (17)–(34) as well as the power regulation constraints discussed earlier. Additionally, due to the reduced time scale of the intraday optimization, this study must consider the constraints on the ALK ramp rate to reflect the ALK start-up characteristics. The specific constraints are as follows:

$$0 \le \Delta P^t_i \le \Delta P^i_{\max} \tag{37}$$

$$\left| P^t_{\mathrm{ALK}} - P^{t-1}_{\mathrm{ALK}} \right| \le dP^{\mathrm{ALK}}_{\max} \tag{38}$$

where $\Delta P^i_{\max}$ denotes the upper limit of power regulation for i, and $dP^{\mathrm{ALK}}_{\max}$ denotes the maximum ramp-up rate of the ALK.

4. Case study and results

4.1. Case description

This paper selects a 110 MW large-scale PV ground power plant in Macheng, Hubei, China, and a 200 MW wind farm from

Goldwind Technology to construct a REHPS. The specific parameters for the WT and PV systems are provided in Tables S1 and S2 in Appendix A. Data for two years (2019–2020) with a 15-min time scale were recorded, and sourced from the publicly available dataset in Ref. [39], which was used in a renewable energy generation prediction competition sponsored by the State Grid of China in 2021.

This paper focuses on the refined modeling and scheduling of components in a one-day HES. Consequently, the configured capacities of each unit, particularly ALK and PEM, must be specified in advance. While a high-capacity electrolyzer can prioritize renewable energy consumption, it comes with high investment costs. The ratio of the two electrolyzers is equally important. A small proportion of PEM may create excessive consumption pressure on ALK, leading to unnecessary wind and solar energy abandonment due to slow response, whereas a larger proportion may result in high costs. Therefore, appropriate capacity allocation increases hydrogen production and wind energy consumption while ensuring that the initial investment cost remains manageable. Ref. [29] explores that a PEM share of 10–20% of the total electrolyzer capacity ensures both a high renewable energy consumption rate and economic efficiency.

To further verify this optimal proportion range, this study conducted a sensitivity analysis on the total electrolyzer capacity (180–240 MW) and PEM proportion (10–25%) in gale weather, as shown in Table 2. The results show that the system achieves the highest total daily net revenue of 94.3 when the total capacity is 220 MW and the PEM proportion is 15%. Within the range of total capacity 200–220 MW and PEM proportion 10–15%, the system's total daily net revenue remains above 93. Therefore, this interval represents the effective distribution range of the system's optimal operating points. Additionally, considering the operating characteristics of ALK and PEM, this study adopts five high-power ALKs (37 MW each, totaling 185 MW) and three low-power PEMs (10 MW each, totaling 30 MW), ensuring that the PEM proportion is optimal. The electrolyzer parameters used in this study are provided in Table 3, and the parameters for other system modules are shown in Table S3 in Appendix A. This study also considers time-of-use tariffs for grid integration, with specific price parameters presented in Table S4 in Appendix A.

To investigate the scheduling optimization of the system under various weather types and enhance robustness, meteorological and power data for three representative weather types (gale, breeze, and cloudy) are selected. A 24-h period within a day is simulated, with 1-h intervals before the day and 15-min intervals within the day for power prediction. The system's mathematical model is then constructed. The MINLP problem is linearized using state transition variables and the Big-M method, integrating the objective functions and constraints of each time scale into a complete MILP parallel solution model. The proposed optimization model is solved using the CPLEX optimizer in MATLAB with multi-threaded parallel computation. The proposed model's approach performs all calculations in tens of seconds. The computing platform used is an AMD Ryzen 9 7900X 12-Core Processor @4.70 GHz with 32 GB RAM.

4.2. Analysis of power forecasting results

4.2.1. Correlation analysis

To obtain more accurate prediction data, this study considers various factors influencing WT and PV power, as shown in Table S5 in Appendix A. These factors are separately correlated, with the linear correlation calculated using PCC and displayed in the correlation heat map in Fig. 8. By comparing the color and size of the thermochromatic blocks in the plot, it is observed that WS_*x* has the highest PCC for WT power, and TSI has the largest for PV power. In other words, wind speed and solar irradiation intensity determine the magnitude of WT and PV power generation, respectively. In this study, data with an absolute PCC value greater than 0.4 are selected as inputs, and unnecessary influences are filtered out for model prediction.

4.2.2. Comparison of the accuracy of different forecasting models

To demonstrate that the proposed CNN–BiLSTM–Attention model performs well on the data, BiLSTM is replaced with LSTM and gated recurrent unit (GRU) for prediction, and model prediction errors are compared. Three methods are used to analyze the predictions based on the proposed weather types. The prediction results are compared with actual results, and the error magnitude is quantified using three technical indices: R^2, mean absolute error (MAE), and root mean square error (RMSE). The results are shown in Fig. 9. It is found that the MAE and RMSE values for the BiLSTM-based prediction are smaller than those of the other methods, and the R^2 is larger, for both WT and PV power, regardless of the weather types. To further verify the model's advancement, additional comparative experiments with baseline models (BiLSTM–Attention, CNN–BiLSTM, BiLSTM, and LSTM) are supplemented. Their prediction performance for WT and PV under different weather types is systematically evaluated (detailed results in Fig. 10). As shown in the boxplots, the proposed model's prediction errors are more concentrated. It achieves the smallest median error and interquartile range for both WT and PV, with fewer outliers. This demonstrates the accuracy and superiority of the proposed method in this study.

4.2.3. Analysis of forecasting results on multi-timescale

As shown in Fig. 11, the joint WT–PV prediction model proposed in this study demonstrates good fitting performance. The prediction accuracy is high for the first two cases: gale and breeze weather, with the latter showing particularly high accuracy. In contrast, the third case shows significant prediction bias at 2, 6, 12, and 24 h, with lower prediction accuracy. This is due to the volatility and uncertainty caused by solar irradiation intensity and gusts in cloudy weather, which increase prediction difficulty and affect the stability of the system's power supply. This explains why PV has higher prediction accuracy than WT, as shown in the figure. Moreover, the short time scale of ultra-short-term intraday predictions reduces volatility and uncertainty, resulting in higher prediction accuracy compared to day-ahead predictions. However, in practical engineering, ultra-high accuracy in ultra-short-term

Table 2
Statistics of TR (104 CNY) for different capacity configurations (gale weather).

Total installed capacity of electrolyzers (MW)	Highest total daily net revenue			
	PEM proportion = 10%	PEM proportion = 15%	PEM proportion = 20%	PEM proportion = 25%
240	92.13	92.67	89.53	86.36
220	93.73	94.30	91.38	88.45
200	93.15	93.71	90.17	89.47
180	92.48	92.88	91.58	90.04

Table 3
Key parameters of ALK and PEM in the system.

Electrolyzer	Configuration number	Rated power (MW)	Percentage of rated power	Ramp rate per minute	Efficiency (%)	Cold start-up time (min)	Warm start-up time (min)	Overload time (min)	Lifespan (a)	Investment cost (CNY·MW^{-1})	O&M cost (CNY·(MW·h)$^{-1}$)
ALK	5	37	20–100%	20%	60–75	60	15	—	15	1.5×10^6	30
PEM	3	10	5–120%	100%	70–85	5	0.1	< 60	10	7.6×10^6	120

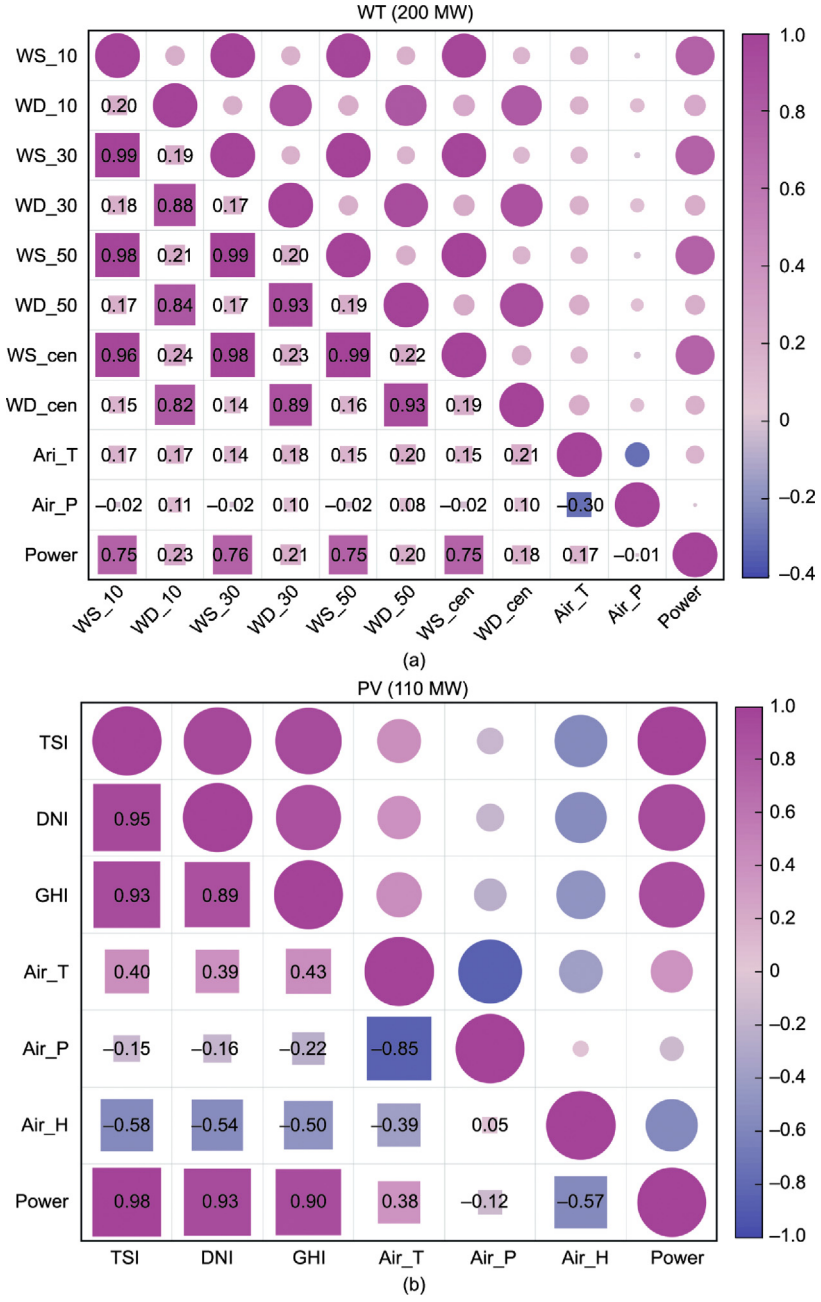

Fig. 8. (a) WT and (b) PV based quantitative analysis of heat maps for PCC. WS_10, 30, and 50: wind speed at height of 10, 30, and 50 m; WD_10, 30, and 50: wind direction at height of 10, 30, and 50 m; WS_cen: wind speed at the height of wheel hub; WD_cen: wind direction at the height of wheel hub; Air_T: air temperature; Air_P: atmosphere; TSI: total solar irradiance; DNI: direct normal irradiance; GHI: global horizontal irradiance; Air_H: relative humidity.

predictions is achieved through intraday real-time prediction, making it impossible to achieve such accuracy a day in advance. Therefore, this study aims to address the challenge of obtaining a stable and efficient HES with a small time-scale response, using the day-ahead prediction with high error as the scheduling plan.

4.3. Analysis of DR results

HLDR is based on the variations in wind and PV power forecasts. Under the influence of load DR, the hydrogen price changes from a fixed value of 35 CNY·kg^{-1} to a fluctuating price. Notably, this vari-

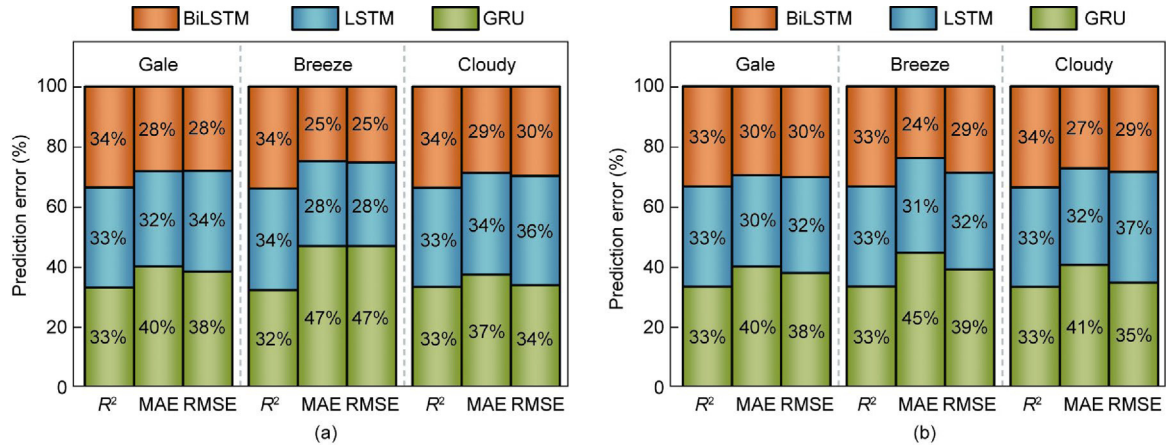

Fig. 9. Comparison of the prediction errors of different forecasting models: comparison of the three evaluation metrics (R^2, MAE, and RMSE) under different weather types: (a) prediction error of WT; (b) prediction error of PV.

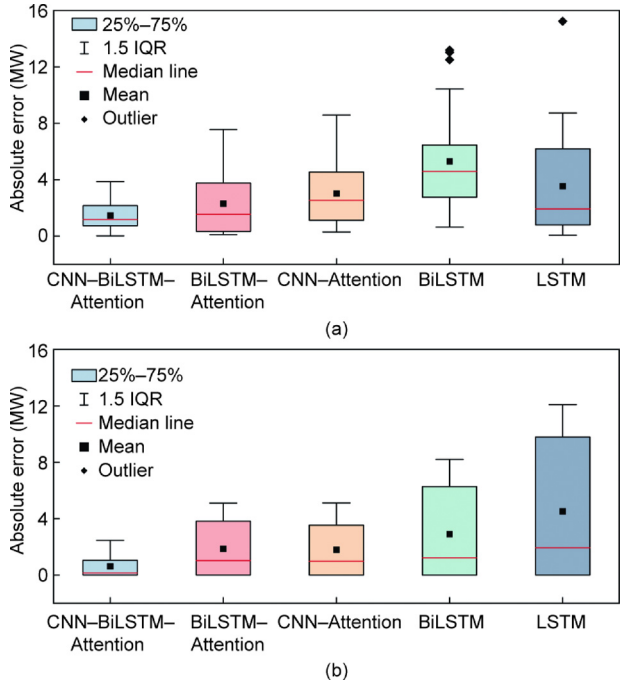

Fig. 10. Absolute error distribution of the five methods: (a) WT; (b) PV. IQR: interquartile range.

ation exhibits an inverse relationship with renewable energy generation power. When wind and solar output is sufficient, hydrogen prices decrease, while they increase during low output, as shown in Fig. 12. However, hydrogen prices do not fluctuate indefinitely with wind and solar power. During gale and cloudy weather, hydrogen prices are constrained between 21–49 CNY·kg^{-1}, while in breeze, they are limited to 31.5–38.5 CNY·kg^{-1}. This is because greater fluctuations in renewable energy output require larger hydrogen price differences to encourage users to purchase more hydrogen when wind and solar output is high and reduce demand when it is low. In contrast, breeze weather is more stable than the other two, resulting in smaller hydrogen price fluctuations and less willingness for users to change their hydrogen consumption habits.

The change in hydrogen prices leads to variations in HL on the user side. This study focuses on analyzing the shiftable and interruptible HLs. The incentive-based policies encourage the reduction of the HL, leading to a decrease in the total HL. As shown in Fig. 12, the HL fluctuates from the previous demand of 1.2 t per time period, exhibiting a negative correlation with hydrogen price changes and a positive correlation with wind and solar power variations. This effectively links the energy supply side with the energy demand side, so that fluctuations and uncertainties on the supply side correspond to changes in the demand side, thus achieving relative stability in the entire renewable energy-based hydrogen production system. To ensure alignment with the actual operational capabilities of the hydrogen energy industry, the minimum time scale for the proposed HLDR solution is set to the day-ahead hourly level. For the intraday phase, the hourly scheduling results are scaled up to a 15-min time scale for application, without fluctuating based on intraday power input. Under the influence of the HLDR proposed in this study, the system's optimization scheduling process is better aligned with hydrogen production efficiency, significantly improving both the stability and efficiency of the hydrogen production system.

4.4. Comparison of optimal scheduling results for different scenarios

This study aims to investigate the performance of the HES and evaluate the superiority of the proposed HLDR and multi-timescale scheduling optimization strategies. In this section, five different hybrid hydrogen production system strategies are evaluated to analyze their optimal system benefits and operational characteristics. The composition of these five case studies is provided in Table 4. It should be noted that all studies are compared under identical physical constraints to ensure a fair baseline comparison, with the specific case studies defined as follows:

Scenario 1: day-ahead scheduling optimization for the ALK-only.

Scenario 2: day-ahead scheduling optimization for the HES.

Scenario 3: day-ahead scheduling optimization for the HES, considering HLDR.

Scenario 4 (proposed): multi-timescale scheduling optimization for the HES, considering HLDR.

Scenario 5: intraday scheduling optimization for the HES, considering HLDR.

4.4.1. Comparative analysis of day-ahead scheduling scenarios

Day-ahead scheduling aims to maximize system economics by providing a highly profitable, smoothed guidance schedule for intraday operations. To better evaluate the scheduling characteristics and economic advantages during the day-ahead phase, Fig. 13 presents the cost and benefits results for Scenarios 1–3 under var-

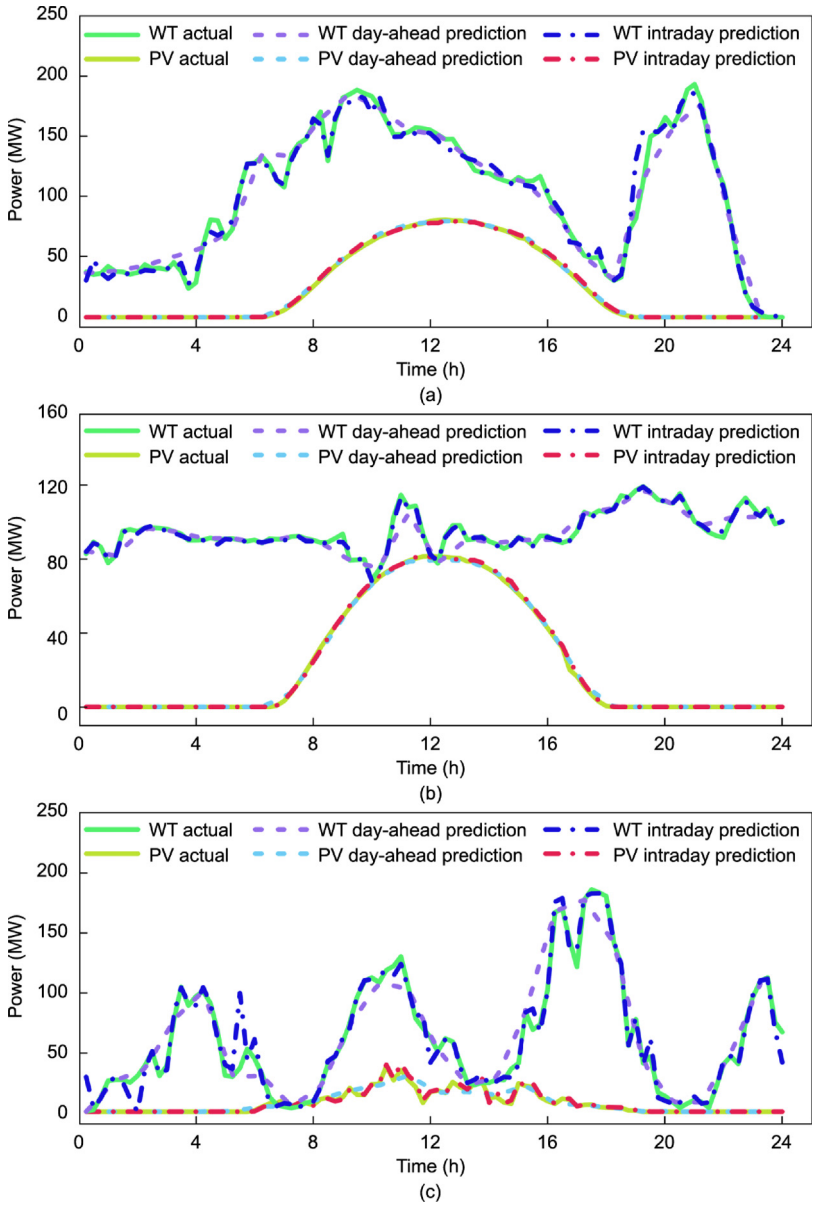

Fig. 11. Multi-timescale forecast results of WT and PV under different weather types during 24 h in a day: (a) gale weather forecasting results; (b) breeze weather forecasting results; (c) cloudy weather forecasting results.

ious weather conditions. The total daily net revenue (TR) is positive for all scenarios, exceeding 200 000 CNY even under severe cloudy conditions, which is crucial for maintaining system sustainability. This demonstrates that the proposed system possesses significant economic value and practical applicability. As shown in Fig. 13, hydrogen revenue (HR) directly reflects the system's hydrogen production capacity, thereby influencing its economic benefits. Notably, the daily TR comprises the economic flows of each subsystem, and coordinating subsystem configurations along with efficient power allocation is essential for scheduling optimization. Based on the system results, it is tentatively concluded that during REHPS operation, the focus should be on increasing hydrogen production capacity in weather conditions with abundant wind and solar resources. Conversely, ensuring system profitability should be accompanied by efforts to maintain stable operations and enhance reliability. This approach maximizes the economic performance of system operations.

To further illustrate the superiority of the HES day-ahead scheduling scheme (Scenario 3) that considers HLDR, the economic values of the different schemes are compared in Table 5. Scenario 1 involves ALK-only hydrogen production, which requires increasing ALK capacity to maintain system stability due to constraints such as slow response and limited operating range. Frequent starts and stops during operation also incur a switching penalty (SW). When comparing Scenario 2 (hybrid hydrogen production) with Scenario 1, and disregarding the similar daily equivalent investment cost (INV), both the return on electricity sales revenue (ER) and HR are improved to varying extents, although the operation and maintenance cost (OM) for Scenario 2 is somewhat higher under different weather conditions. Furthermore, the introduction of PEM eliminates the economic losses caused by SW by assisting in maintaining smooth hydrogen production at ALK. Ultimately, the TR of Scenario 2 improves by nearly 5% under conditions with abundant wind and solar resources, and can increase by up to 25%

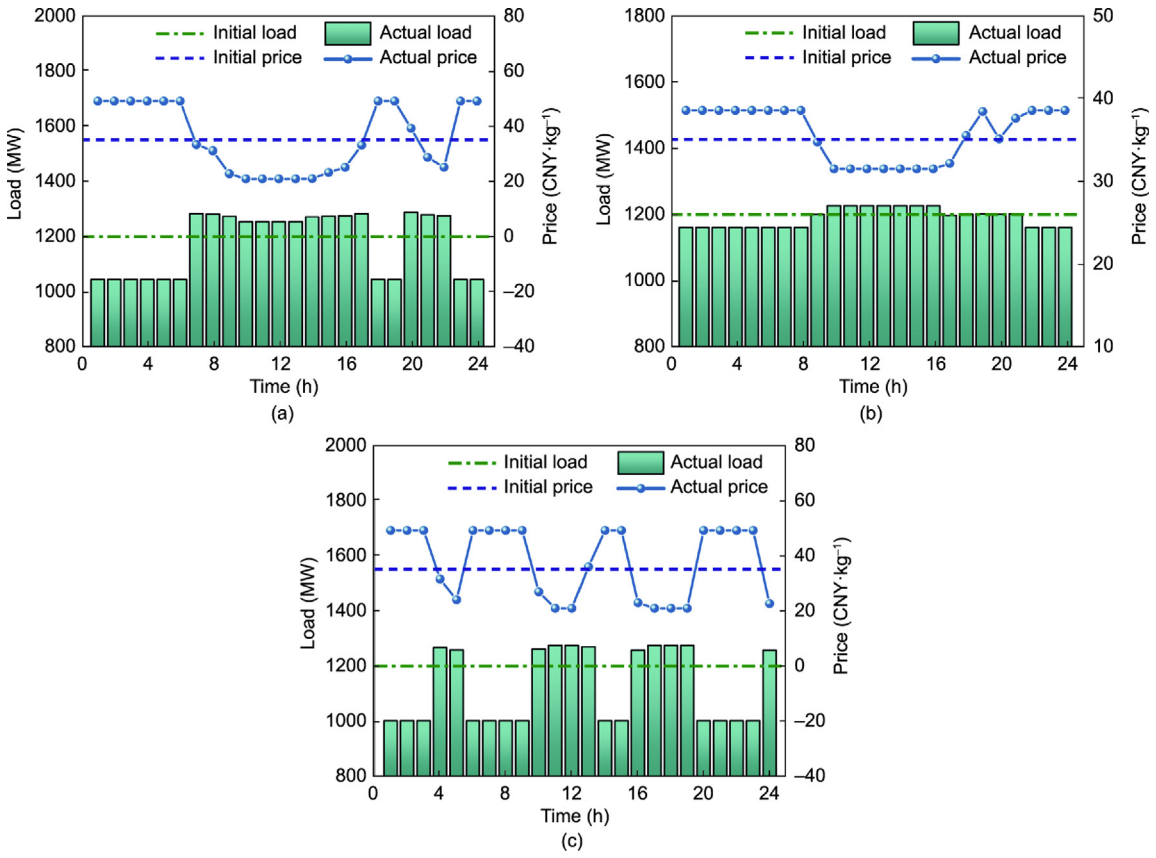

Fig. 12. Response of HL and hydrogen price after the adoption of HLDR under different weather types during 24 h in a day: (a) gale weather; (b) breeze weather; and (c) cloudy weather.

Table 4
Composition of the case studies.

Scenario	ALK	PEM	HLDR	Hour-time scale	15 min-time scale	Objectives
1	√	–	–	√	–	max C_{Profit}
2	√	√	–	√	–	max C_{Profit}
3	√	√	√	√	–	max C_{Profit}
4	√	√	√	√	√	min $C_{Penalty}$
5	√	√	√	–	√	max C_{Profit}

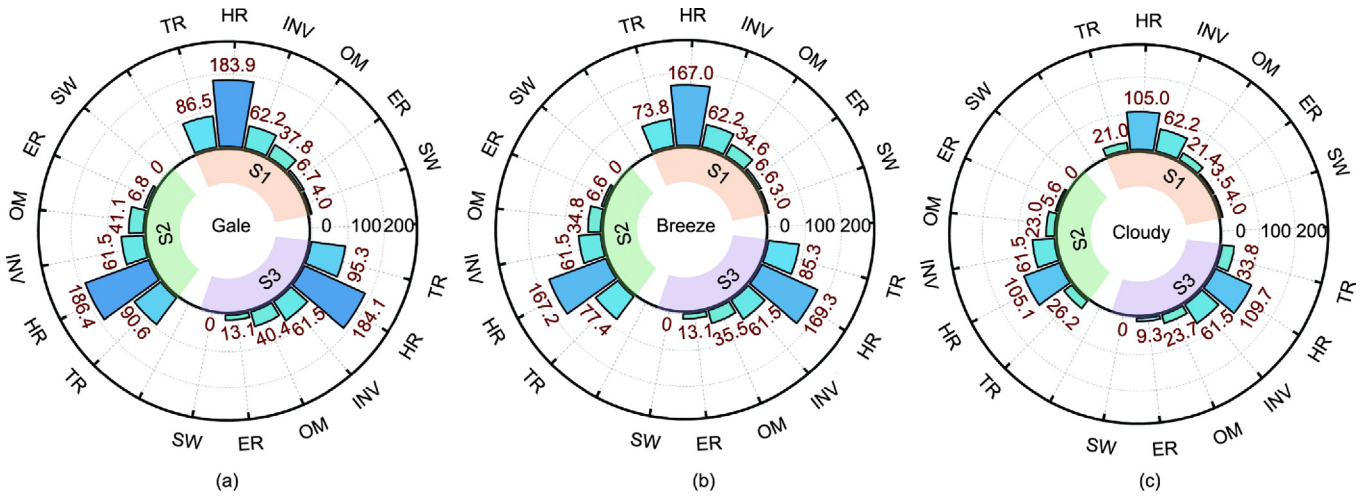

Fig. 13. Comparison of the economics of Scenarios 1–3 for 24 h in a day under different weather types: (a) gale weather; (b) breeze weather; and (c) cloudy weather.

Table 5
Comparison of the economics for 24 h in a day under different Scenarios 1–3.

Parameter ($\times 10^4$ CNY)	Gale			Breeze			Cloudy		
	S1	S2	S3	S1	S2	S3	S1	S2	S3
Hydrogen sales revenue (C_{HR})	183.9	186.4	184.1	167.0	167.2	169.3	105.0	105.1	109.7
Electricity trading revenue (C_{ER})	6.7	6.8	13.1	6.6	6.6	13.1	3.5	5.6	9.3
Operation and maintenance costs (C_{OM})	37.8	41.1	40.4	34.6	34.8	35.5	21.4	23.0	23.7
Equivalent investment costs (C_{INV})	62.2	61.5	61.5	62.2	61.5	61.5	62.2	61.5	61.5
switching penalty (C_{SW})	4.0	0	0	3.0	0	0	4.0	0	0
Total net revenue (C_{TR})	86.5	90.6	95.3	73.8	77.4	85.3	21.0	26.2	33.8

under extreme weather. HES renders REHPS more flexible, enabling full utilization of RES and enhancing resilience to uncertainties and disturbances. This, in turn, demonstrates the superior economic efficiency of HES, particularly under severe weather conditions.

To demonstrate the economic improvements brought by HLDR, Scenario 2 is compared with Scenario 3. Previous analysis shows that introducing HLDR causes HLs to vary in line with renewable generation trends, greatly enhancing the flexibility of system power flow. As illustrated in Fig. 13, Scenario 3 can utilize MG for power trading more flexibly while maintaining high HR, with ER nearly doubling. This economic growth generally scales linearly with HL responsiveness, becoming more pronounced during periods of abundant wind and solar resources. Relevant sensitivity analyses are presented in Table S6 in Appendix A. The introduction of HLDR enables the entire REHPS to flexibly deploy its subsystems from multiple perspectives and optimize scheduling with a focus on high economic efficiency. Ultimately, the proposed day-ahead scheduling strategy (Scenario 3) is verified as the optimal plan.

4.4.2. Analysis of energy flow scheduling on multi-timescale

Taking Scenario 3 as the day-ahead scheduling plan, the proposed intraday rolling optimization strategy at a 15-min scale is designated as Scenario 4. Fig. 14 presents the multi-timescale energy flow scheduling results for both day-ahead and intraday phases. The overall energy flow scheduling mechanism is as follows: ALK, serving as the primary power consumer and hydrogen production unit, operates stably throughout the entire period; PEM, acting as the auxiliary hydrogen production unit, adjusts its output to sustain stable hydrogen production in ALK during peaks or drastic fluctuations in renewable power generation; MG adjusts grid transactions based on daily electricity price fluctuations and renewable energy generation availability—typically buying power at night when prices are low and selling during the day when prices are high—to maintain high system efficiency and ensure stable, effective operation; and battery's flexible regulation capability proves valuable in scenarios with smaller-scale power generation and larger fluctuations, where more frequent charging and discharging are needed to meet energy conservation objectives.

To explore the key role of intraday rolling optimization, the synchronous operation of day-ahead and intraday scheduling under identical weather conditions is compared. First, day-ahead forecast errors are inevitable, particularly under severe weather conditions where drastic power fluctuations are challenging to predict accurately. In intraday dispatch, a rolling optimization strategy is employed to adjust energy flow allocation and enhance the system's resilience by incorporating ultra-short-term forecasts of WT–PV generation. When power deviates from the day-ahead forecast, each unit adjusts its output with minimal modification to accommodate fluctuations. A comparison of power changes across different time scales reveals that the overall trend adheres to the day-ahead scheduling plan, although adjustments occur to varying degrees at finer scales. The challenge of achieving smooth scheduling at finer scales is overcome, thereby balancing the economic performance and stability of REHPS.

To analyze the independent operation and schedule execution of each electrolyzer in the HES under Scenario 4, Fig. 15 illustrates the operation of individual ALKs and PEMs under day-ahead scheduling and intraday rolling optimization. The coordinated power allocation among electrolyzers enables each unit to participate in system regulation without excessive pressure, promoting system stability. The day-ahead schedules of individual electrolyzers become smoother at finer time scales, enabling periodic execution under varying weather conditions. Regarding overall consistency with the planning curve, the execution rate of the day-ahead plan for each electrolyzer under different weather conditions exceeds 96%, demonstrating the effectiveness and accuracy of the proposed scheme. Large deviations at certain moments (e.g., 18:30 in gale weather and 2:00, 11:00 in cloudy weather) result from sudden intraday weather changes, preventing the day-ahead plan from ensuring normal system operation. During this process, the faster start–stop capability of PEMs allows them to prioritize power regulation, preventing deviations from the day-ahead plan caused by ALK downtime and accumulated errors. The proposed strategy effectively maximizes hydrogen production capacity and enhances the robustness of the HES.

4.4.3. Advantages of multi-timescale scheduling optimization

To quantify the advantages of the proposed multi-timescale scheduling strategy (Scenario 4), a scheduling scheme with optimal intraday economic performance (Scenario 5) is established for comparison. Scenario 5 optimizes scheduling by using the forecasted power of ultrashort-term renewable generation as input and directly maximizing intraday TR as the objective. This strategy used in Scenario 5 is the economics optimization approach that is currently dominant in the relevant literature. This strategy neglects irreversible economic losses from frequent electrolyzers' load changes and the time-dependent degradation of ultrashort-term forecasts, aiming to achieve the maximum economic benefit for Scenario 4 under identical mathematical constraints.

Table 6 presents the economic results for Scenarios 4 and 5. The proposed strategies demonstrate high economic efficiency under various weather conditions, supported by a stable and efficient multi-timescale hydrogen production strategy. As a result, the TR of Scenario 4 arrives at 98% of the ideal Scenario 5 under gale and breeze conditions and remains above 80% even in extreme cloudy weather. This result strongly validates the economic advantages of the multi-timescale scheduling strategy.

The power flow of Scenarios 4 and 5 is analyzed in Fig. 16. Scenario 5 achieves high economic efficiency by operating ALK at high loads. However, this approach causes long-term irreversible degradation of ALK and fails to leverage the flexibility of REHPS's multiple subsystems. In contrast, Scenario 4 optimizes the energy flow distribution by reducing unnecessary ALK output, enhancing system flexibility. As shown in the figure, Scenario 4 significantly increases the energy utilization of battery charging, PEM consumption, and energy sold to MG, except under cloudy weather, where the energy sold to MG is lower than in Scenario 5. This is because, under extreme weather conditions with large power fluctuations, energy is prioritized for maintaining system stability, naturally

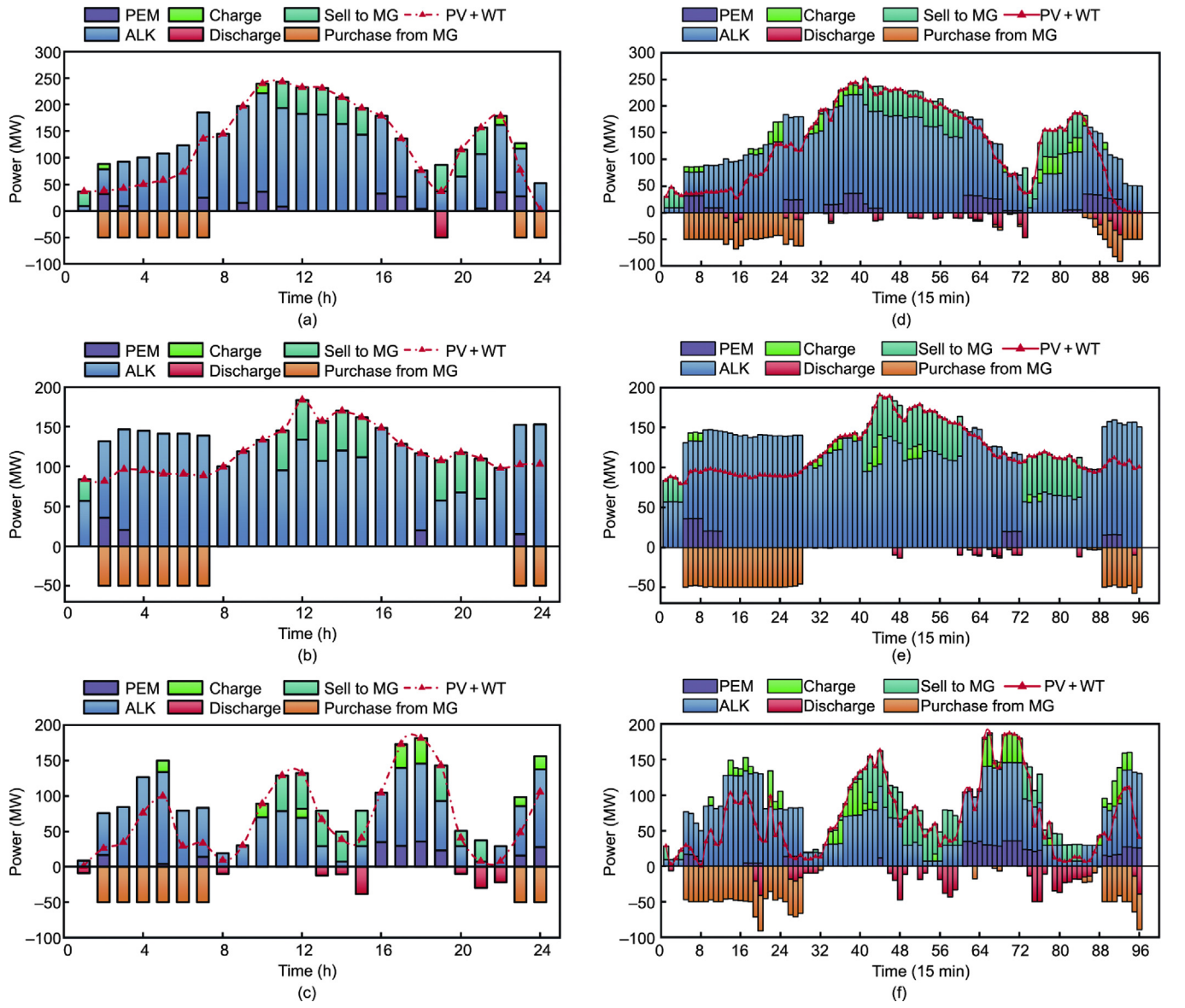

Fig. 14. Scheduling optimization results at multi-timescale for 24 h in a day under different weather types. Day-ahead scheduling results in (a) gale weather, (b) breeze weather, and (c) cloudy weather; intraday scheduling results in (d) gale weather, (e) breeze weather, and (f) cloudy weather.

reducing the amount sold to the external grid. This effect is reflected in the ER shortfall under cloudy weather in Table 6, leading to a significant decrease in overall TR. The coordination of REHPS's multiple subsystems is crucial for system operation and disturbance resistance, highlighting the flexibility advantages of the multi-timescale scheduling strategy.

Fig. 17 illustrates the 24-h operating loads of each electrolyzer in Scenario 5. Without a scheduling plan, the electrolyzer outputs fluctuate significantly, frequently adjusting loads to maximize economic efficiency at each time scale. Prolonged operation accelerates electrolyzer degradation, lowers hydrogen production efficiency, reduces adaptability to extreme weather, and results in irreversible losses. In contrast, Scenario 4, under the same weather conditions in Fig. 15, significantly reduces frequent load variations while also minimizing some start-stop behavior. The smooth operation of electrolyzers highlights the multi-timescale scheduling strategy's advantage in ensuring system stability.

To enable a more robust assessment of the proposed strategy's effectiveness, WT and PV power generation data from 8 to 14 April 2020 are used as system inputs. Model validation is performed over this one week, capturing a wider range of weather conditions. Fig. 18 presents the execution rates of the operational plans for each electrolyzer. The results show that, while maintaining high economic efficiency, the average execution rate of each electrolyzer's previous-day plan reached 97.9%. This further confirms the effectiveness and operational stability of the proposed strategy.

To further reinforce the reliability of the conclusions, a sensitivity analysis is conducted on key economic parameters (operational and maintenance costs for ALK and PEM, base HL, hydrogen price, electricity price, and maximum grid power) with ±10% and ±20% adjustments around baseline values under typical gale weather. Detailed analysis results are presented in Table S7 in Appendix A. Results indicate that the system's TR remains positive across all scenarios except the hydrogen price, with fluctuations within 6%. Notably, HR accounts for the largest share of the system's TR, making TR highly sensitive to hydrogen price fluctuations [25]. The multi-timescale scheduling strategy effectively mitigates the impacts of parameter variations, ensuring the stable operation of

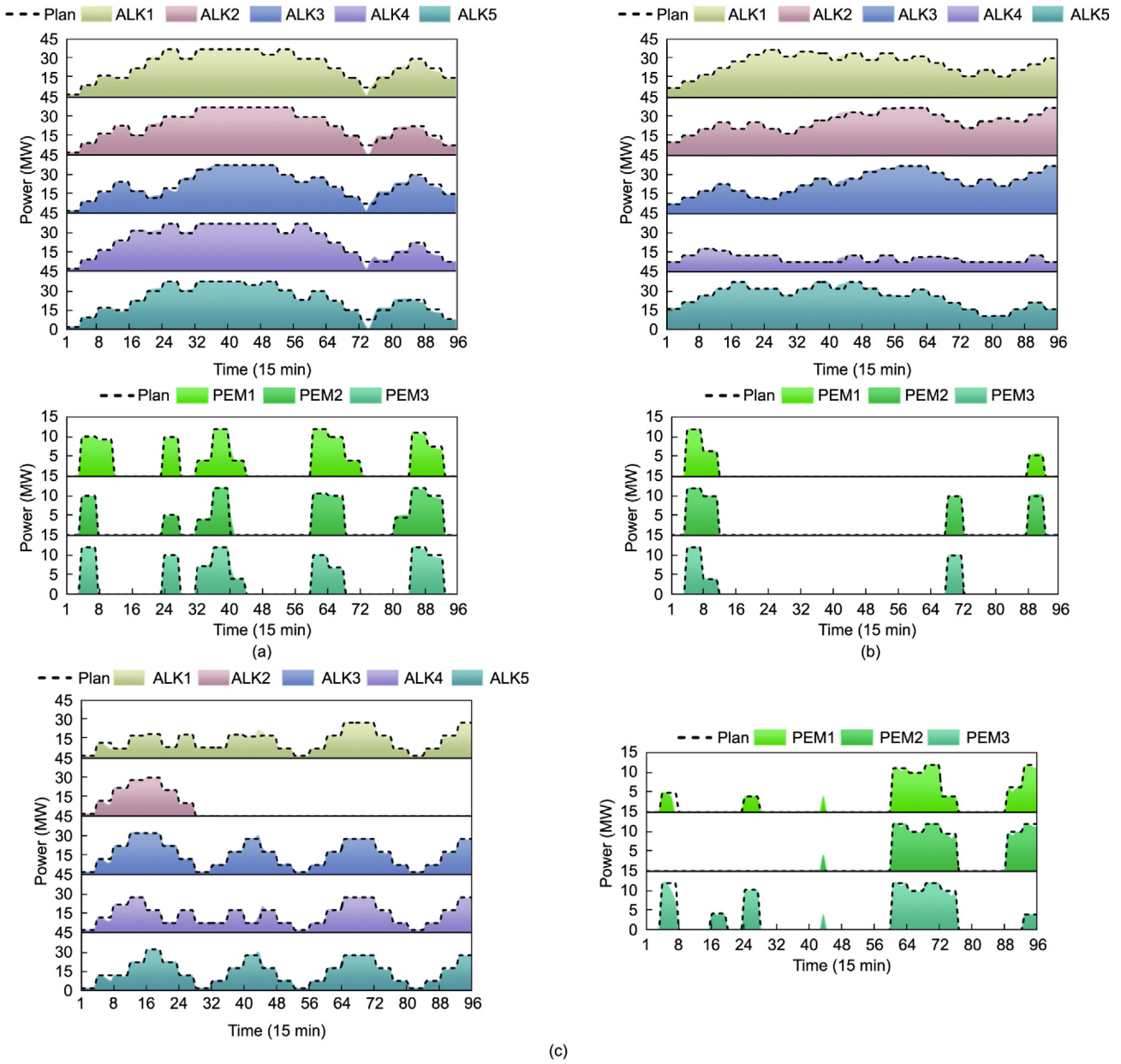

Fig. 15. Execution status of the operational plan for each electrolyzer in the HES for 24 h in a day under different weather types: (a) gale weather, (b) breeze weather, and (c) cloudy weather.

Table 6
Comparison of the economics of Scenarios 4 and 5 for 24 h in a day under different weather types.

Parameter ($\times 10^4$ CNY)	Scenario 4			Scenario 5		
	Gale	Breeze	Cloudy	Gale	Breeze	Cloudy
Hydrogen sales revenue (C_{HR})	180.12	168.29	102.45	179.35	170.22	102.74
Electricity trading revenue (C_{ER})	10.68	12.45	7.10	10.97	11.00	10.15
Operation and maintenance costs (C_{OM})	40.33	35.94	23.77	38.45	35.56	21.71
Equivalent investment costs (C_{INV})	61.53	61.53	61.53	61.53	61.53	61.53
Total net revenue (C_{TR})	88.94	83.27	24.25	90.33	84.12	29.65

all system components (execution rate ≥ 96%) across all scenarios, thus verifying the robustness of the proposed strategy.

5. Conclusions

This paper optimizes the multi-timescale scheduling of REHPS by integrating WT and PV generation power forecasting, HLDR, and incorporating ALK, PEM, MG, battery, and HST. We develop a joint WT–PV forecasting model based on CNN–BiLSTM–Attention, along with flexible HL price-based and incentive-based DR models. Multi-state refined modeling is applied to the HES consisting of ALKs and PEMs. The joint constraints are incorporated into a MILP model using state-variable control and the Big-M method. In the day-ahead phase, the objective of optimal scheduling is the maximization of total system revenue, primarily driven by hydrogen production capacity. During the intraday phase, the day-ahead

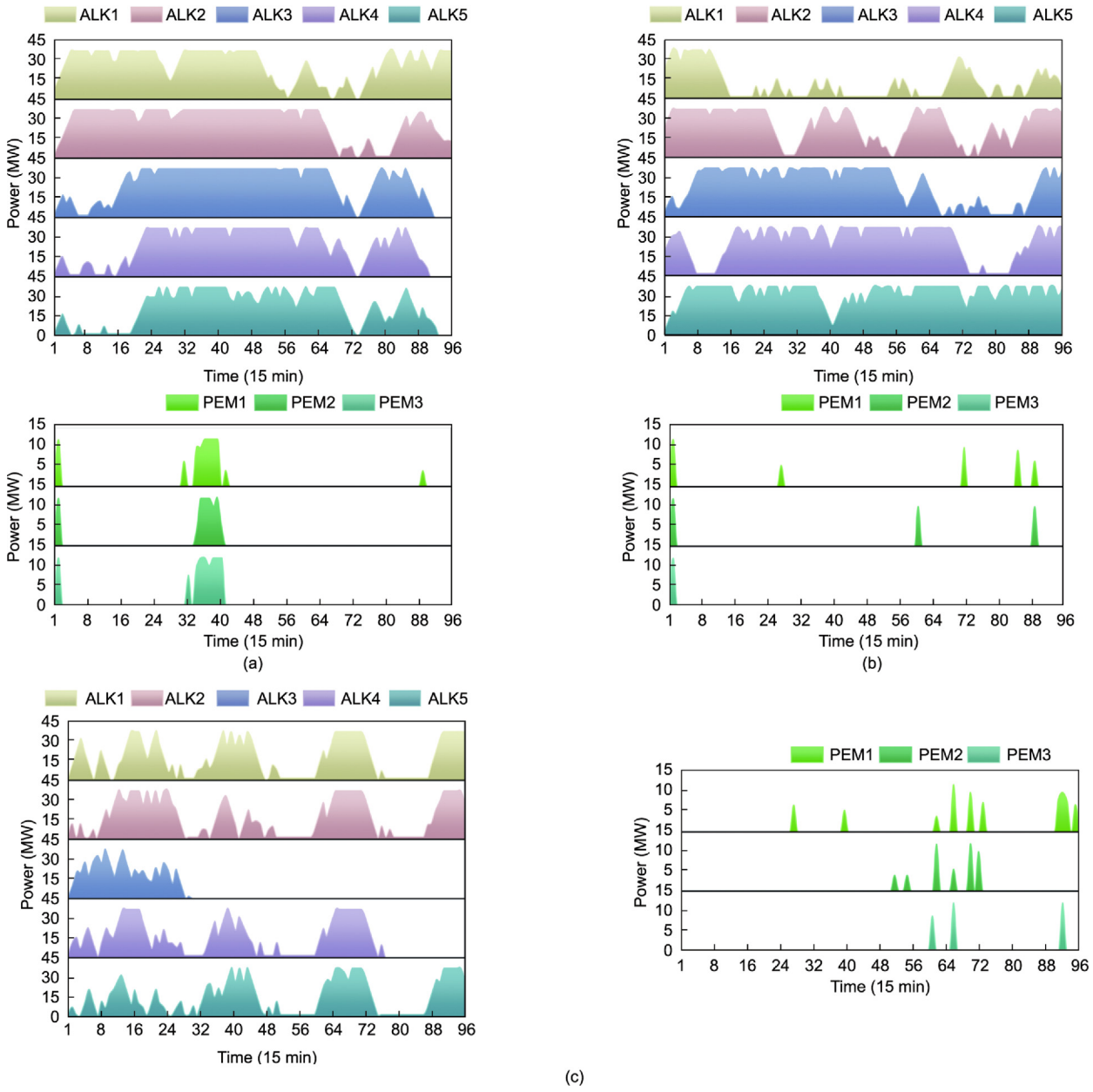

Fig. 17. Operational load of each electrolyzer in the HES in Scenario 5 for 24 h in one day under different weather types: (a) gale weather, (b) breeze weather, and (c) cloudy weather.

scheduling plan guides the optimization process, which is continuously adjusted using real-time, small-scale forecasting information. The optimal scheduling and economic benefits of the HES are analyzed using a case study of a PV and a wind farm in Macheng, Hubei, China. The study investigates the impacts of various weather types and scenarios on the system and the operating status of individual electrolyzers. The main conclusions of this study are summarized below:

(1) The CNN–BiLSTM–Attention model accurately predicts the variations in generation power of WT and PV, demonstrating strong fitting ability. This modeling approach outperforms both advanced counterparts (CNN–LSTM–Attention, CNN–GRU–Attention) and baseline models (BiLSTM–Attention, CNN–BiLSTM, BiLSTM, LSTM) in stability and error control across various weather types.

(2) The introduction of PEM ensures stable hydrogen production from ALK while preventing frequent start–stop cycles. The TR of hybrid hydrogen production increases by 5% under sufficient wind and solar resources and up to 25% in extreme weather conditions. HES maximizes renewable energy utilization while improving system resilience to disturbances.

(3) HLDR allows the energy demand side to adapt to supply fluctuations through time-of-use hydrogen pricing and incentives. The system flexibly deploys subsystems, increasing MG power trading while maintaining high HR and nearly doubling ER.

(4) The intraday rolling optimization strategy enhances HES's hydrogen production capacity and robustness, achieving an execution rate of over 96% for each electrolyzer under different weather conditions.

(5) Compared to the ideal maximum economy, the multi-timescale scheduling strategy achieves 98% economic efficiency in calm weather and 80% in extreme weather. It also offers distinct advantages in system flexibility and stability, ensuring REHPS's stable operation.

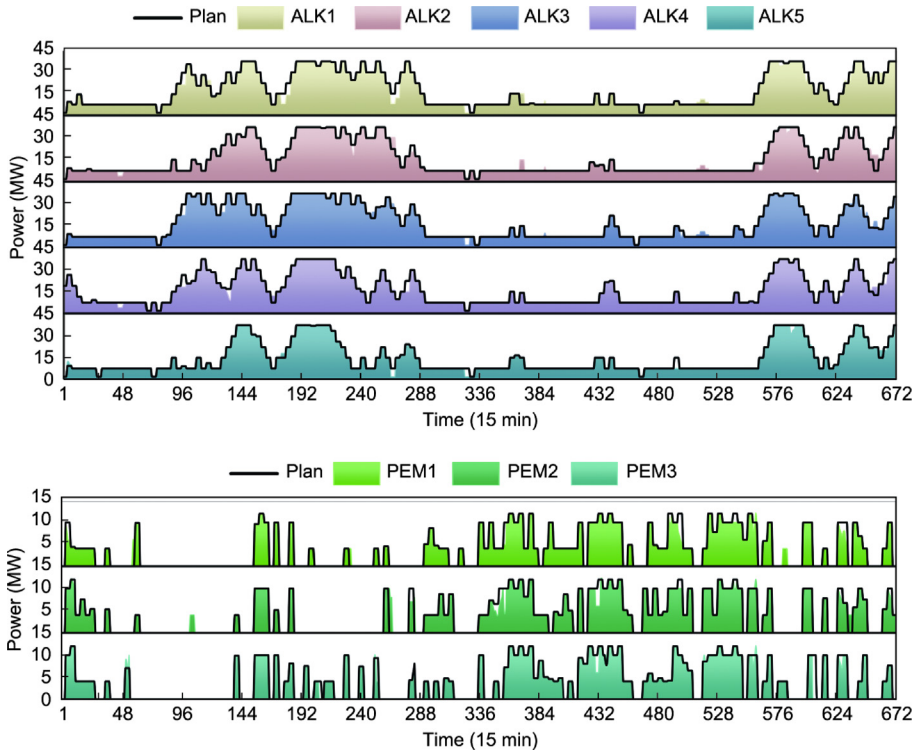

Fig. 18. Execution status of the operational plan for each electrolyzer in the HES for 168 h in a week under different weather types.

These conclusions indicate that coupling HES with HLDR significantly enhances hydrogen production capacity, economic efficiency, and stable operation through the adoption of a multi-timescale optimal scheduling strategy. This approach provides an effective solution for the optimal scheduling of REHPS. The proposed strategy is both promising and scalable. The method is not only applicable to hydrogen production systems but can also be extended to integrated energy systems, hydrogen refueling stations, fuel cells, and other hydrogen utilization scenarios. A stable hydrogen supply strategy supports the optimization and upgrading of the energy structure. This connection between hydrogen production optimization and end-use utilization enhances the practical significance of the proposed strategy in promoting the hydrogen energy industry chain. However, optimizing the hydrogen supply chain at a larger system scale remains challenging due to the inherent difficulties in hydrogen storage and transportation. Future studies will focus on developing highly efficient strategies for the long-term operation of the HES using ALK and PEM, as well as enhancing its robustness against disturbances using stochastic robust optimization.

CRediT authorship contribution statement

Bowen Wang: Writing – original draft, Visualization, Methodology, Data curation, Conceptualization. **Zhaoqing Liang:** Writing – review & editing, Methodology, Data curation, Conceptualization. **Kai Yang:** Visualization, Data curation. **Lei Xing:** Methodology, Formal analysis. **Heng Shao:** Methodology, Formal analysis. **Zhuorui Wu:** Validation, Investigation. **Yixin Liu:** Supervision, Formal analysis. **Li Guo:** Methodology, Investigation. **Ning Yang:** Validation, Investigation. **Bing Hu:** Software, Conceptualization. **Chengshan Wang:** Supervision, Resources, Formal analysis. **Kui Jiao:** Writing – review & editing, Supervision, Resources, Methodology, Formal analysis, Data curation.

Declaration of competing interest

The authors declare that they have no known competing financial interests or personal relationships that could have appeared to influence the work reported in this paper.

Acknowledgments

This work was supported by the National Natural Science Foundation of China for Distinguished Young Scholars (52225604).

Appendix A. Supplementary data

Supplementary data to this article can be found online at https://doi.org/10.1016/j.eng.2026.02.020.

References

[1] Bravo R, Ortiz C, Chacartegui R, Friedrich D. Multi-objective optimisation and guidelines for the design of dispatchable hybrid solar power plants with thermochemical energy storage. Appl Energy 2021;282:116257.
[2] Li Q, Zhou Y, Wei F, Li S, Wang Z, Li J, et al. Multi-time scale scheduling for virtual power plants: integrating the flexibility of power generation and multi-user loads while considering the capacity degradation of energy storage systems. Appl Energy 2024;362:122980.
[3] Egging-Bratseth R, Kauko H, Knudsen BR, Bakke SA, Ettayebi A, Haufe IR. Seasonal storage and demand side management in district heating systems with demand uncertainty. Appl Energy 2021;285:116392.
[4] Parra D, Valverde L, Pino FJ, Patel MK. A review on the role, cost and value of hydrogen energy systems for deep decarbonisation. Renew Sustain Energy Rev 2019;101:279–94.
[5] Yang B, Zhang Z, Su S, Li J, Wang J, Zhang R, et al. Optimal scheduling of wind–photovoltaic–hydrogen system with alkaline and proton exchange membrane electrolyzer. J Power Sources 2024;614:235010.
[6] Chi Y, Li R, Li J, Yang S. The innovation consumption mode of distributed renewable energy under resource bricolage: a case study of China. Energy Rep 2024;11:1420–9.
[7] Macedo SF, Peyerl D. Prospects and economic feasibility analysis of wind and solar photovoltaic hybrid systems for hydrogen production and storage: a case

study of the Brazilian electric power sector. Int J Hydrog Energy 2022;47(19):10460–73.
[8] Lu X, Du B, Zhou S, Zhu W, Li Y, Yang Y, et al. Optimization of power allocation for wind-hydrogen system multi-stack PEM water electrolyzer considering degradation conditions. Int J Hydrog Energy 2023;48(15):5850–72.
[9] Du B, Zhu S, Zhu W, Lu X, Li Y, Xie C, et al. Energy management and performance analysis of an off-grid integrated hydrogen energy utilization system. Energy Convers Manag 2024;299:117871.
[10] Arsad AZ, Hannan MA, Al-Shetwi AQ, Mansur M, Muttaqi KM, Dong ZY, et al. Hydrogen energy storage integrated hybrid renewable energy systems: a review analysis for future research directions. Int J Hydrog Energy 2022;47(39):17285–312.
[11] Guan D, Wang B, Zhang J, Shi R, Jiao K, Li L, et al. Hydrogen society: from present to future. Energy Environ Sci 2023;16(11):4926–43.
[12] Zhang Q, Xie D, Zeng Y, Liu Y, Yu H, Liu S. Optimizing wind-solar hydrogen production through collaborative strategy with ALK/PEM multi-electrolyzer arrays. Renew Energy 2024;232:121116.
[13] Zhao Y, Chen C, Teng M, Zhong J, Sun X. Refined modeling and approximated aggregation method for alkaline water electrolyzers in power system optimal scheduling. Int J Hydrog Energy 2024;52:200–12.
[14] Benghanem M, Almohamadi H, Haddad S, Mellit A, Chettibi N. The effect of voltage and electrode types on hydrogen production powered by photovoltaic system using alkaline and PEM electrolyzers. Int J Hydrog Energy 2024;57:625–36.
[15] Xu Y, Cai S, Chi B, Tu Z. Technological limitations and recent developments in a solid oxide electrolyzer cell: a review. Int J hydrog energy 2024;50:548–91.
[16] Mucci S, Mitsos A, Bongartz D. Power-to-X processes based on PEM water electrolyzers: a review of process integration and flexible operation. Comput Chem Eng 2023;175:108260.
[17] Norazahar N, Khan F, Rahmani N, Ahmad A. Degradation modelling and reliability analysis of PEM electrolyzer. Int J Hydrog Energy 2024;50:842–56.
[18] Xu G, Wu Y, Tang S, Wang Y, Yu X, Ma M. Optimal design of hydrogen production processing coupling alkaline and proton exchange membrane electrolyzers. Energy 2024;302:131827.
[19] Ursúa A, Barrios EL, Pascual J, Martín IS, Sanchis P. Integration of commercial alkaline water electrolysers with renewable energies: limitations and improvements. Int J Hydrog Energy 2016;41(30):12852–61.
[20] Ibáñez-Rioja A, Järvinen L, Puranen P, Kosonen A, Ruuskanen V, Hynynen K, et al. Off-grid solar PV–wind power–battery–water electrolyzer plant: simultaneous optimization of component capacities and system control. Appl Energy 2023;345:121277.
[21] Marocco P, Ferrero D, Lanzini A, Santarelli M. Optimal design of stand-alone solutions based on RES + hydrogen storage feeding off-grid communities. Energy Convers Manag 2021;238:114147.
[22] Huang W, Zhang B, Ge L, He L, Liao W, Ma P. Day-ahead optimal scheduling strategy for electrolytic water to hydrogen production in zero-carbon parks type microgrid for optimal utilization of electrolyzer. J Energy Storage 2023;68:107653.
[23] Ren Y, Jin K, Gong C, Hu J, Liu D, Jing X, et al. Modelling and capacity allocation optimization of a combined pumped storage/wind/photovoltaic/hydrogen production system based on the consumption of surplus wind and photovoltaics and reduction of hydrogen production cost. Energy Convers Manag 2023;296:117662.
[24] Ali ZM, Calasan M, Aleem SHEA, Jurado F, Gandoman FH. Applications of energy storage systems in enhancing energy management and access in microgrids: a review. Energies 2023;16(16):5930.
[25] Dong XJ, He GX, Zhou ZW, Shen JN, He YJ. Simultaneous design and scheduling optimization of the photovoltaic–wind–hydropower–hydrogen hybrid system. Energy Convers Manag 2024;314:118638.
[26] Zheng B, Bai Z, Yuan Y, Hu W. Hydrogen production system and capacity optimization based on synergistic operation with multi-type electrolyzers under wind–solar power. Proc CSEE 2022;42(23):8486–96.
[27] Lin J, Hao W, Ban M. Configuration Optimization of hybrid electrolyzer for wind-based green hydrogen production system. In: 2024 IEEE 7th international electrical and energy conference, 2024 May 10–12, Harbin, China. IEEE; 2024. p. 4734–40.
[28] Lu Y, Yang G, Li X, Liu J, Yang T, Liu J. Dynamic power allocation for the new energy hybrid hydrogen production system based on WOA–VMD: improving fluctuation balance and optimizing control strategy. Int J Hydrog Energy 2024;94:580–99.
[29] Yu B, Fan G, Sun K, Chen J, Sun B, Tian P. Adaptive energy optimization strategy of island renewable power-to-hydrogen system with hybrid electrolyzers structure. Energy 2024;301:131508.
[30] Hu S, Guo B, Ding S, Yang F, Dang J, Liu B, et al. A comprehensive review of alkaline water electrolysis mathematical modeling. Appl Energy 2022;327:120099.
[31] Zhang J, Liu Z. Low carbon economic scheduling model for a park integrated energy system considering integrated demand response, ladder-type carbon trading and fine utilization of hydrogen. Energy 2024;290:130311.
[32] Wang Z, Du B, Li Y, Xie C, Wang H, Huang Y, et al. Multi-time scale scheduling optimization of integrated energy systems considering seasonal hydrogen utilization and multiple demand responses. Int J Hydrog Energy 2024;67:728–49.
[33] Kirschen DS, Strbac G, Cumperayot P, de Paiva MD. Factoring the elasticity of demand in electricity prices. IEEE Trans Power Syst 2000;15(2):612–7.
[34] Li P, Wang Z, Wang J, Guo T, Yin Y. A multi-time-space scale optimal operation strategy for a distributed integrated energy system. Appl Energy 2021;289:116698.
[35] Ma X, Peng B, Ma X, Tian C, Yan Y. Multi-timescale optimization scheduling of regional integrated energy system based on source–load joint forecasting. Energy 2023;283:129186.
[36] Hu J, Tong Y, Liu X, Wang J, Xu Y. Multi-time-scale robust optimization strategy for integrated energy systems considering refined hydrogen energy utilization. Trans China Electrotech Soc 2024;39(5):1419–35.
[37] Dong XJ, Shen JN, Liu CW, Ma ZF, He YJ. Simultaneous capacity configuration and scheduling optimization of an integrated electrical vehicle charging station with photovoltaic and battery energy storage system. Energy 2024;289:129991.
[38] Zhao YB, Dong XJ, Shen JN, He YJ. Simultaneous sizing and scheduling optimization for PV–wind–battery hybrid systems with a modified battery lifetime model: a high-resolution analysis in China. Appl Energy 2024;360:122812.
[39] Chen Y, Xu J. Solar and wind power data from the Chinese state grid renewable energy generation forecasting competition. Sci Data 2022;9(1):577.